Role of the low-frequency deformation field on the explosive growth of extratropical cyclones at the jet exit. Part I: barotropic critical region

G. Rivière* and A. Joly

Centre National de Recherches Météorologiques, Météo-France, Toulouse, France

November 24, 2004

Submitted

---

*Corresponding author: Geophysical Fluid Dynamics Laboratory, Princeton University, Forrestal Campus, P.O Box 308, Princeton, NJ 08542, USA; E-mail: griviere@princeton.edu

Abstract

By using new theoretical results on perturbation growth in spatially and temporally complex quasigeostrophic flows, this paper investigates the role of the large-scale deformation field on the explosive growth of extratropical cyclones in the jet-exit region. Theoretical ideas are tested by analyzing FASTEX reanalysis data during February 1997 and by decomposing the atmospheric flow into a high and a low-frequency part corresponding respectively to the synoptic signal and the large-scale flow.

Regions where the low-frequency deformation magnitude is greater than the absolute value of the low-frequency relative vorticity are shown to be dynamically relevant as these regions in the upper-troposphere, which are intrinsically related to the horizontal inhomogeneities of the low-frequency upper-tropospheric jet, correspond to regions where synoptic disturbances tend to be located.

In the jet-exit region of mid-february 1997, the boundary between two of these regions, one located on the anticyclonic side of the jet and another downstream on the cyclonic one is shown to be the preferred region where synoptic eddies tend to cross the jet from the south to the north and is called a barotropic critical region. A detailed analysis of IOP17 of FASTEX during its crossing of the jet around the barotropic critical region is performed. Two processes explain the IOP17 development during the crossing. One involves the barotropic generation rate whose sign is completely modified with the sudden change of the dilatation axes orientation around the barotropic critical region. The other one is baroclinic interaction which is strongly maintained far away from the baroclinicity maximum due to a new favourable baroclinic configuration. A new mechanism is proposed to explain this favourable baroclinic configuration involving the barotropic processes in the low levels during the crossing of the jet.

1 Introduction

Many observational evidences show that the large-scale flow related to the jet streams plays a crucial role on the shape, growth and trajectories of midlatitude cyclones (Evans et al., 1994; Young, 1995; Schultz et al., 1998; Ayrault, 1998 among others) and more generally of all transient synoptic eddies at different levels (e.g., Lau, 1988; Sickmoller et al., 2000). While the jet stream baroclinicity is the main source of energy for synoptic eddies growth, numerous numerical studies have shown that its horizontal inhomogeneities, or in other words the large-scale barotropic deformation field, modulates synoptic eddies growth rates and their location; studies from Hoskins and West (1979), Simmons and Hoskins (1980), James (1987), Davies et al. (1991), Barcilon and Bishop (1998) exhibit this result in zonal sheared flows while the works of Shutts (1983), Pierrehumbert (1984), Cai and Mak (1990), Whitaker and Barcilon (1992) and Bishop (1993) show it in zonally varying or confluent/diffluent flows. Thorncroft et al (1993) show also that introducing an asymetry between the cyclonic and anticyclonic parts of the zonal jet leads to very different baroclinic eddy life cycles. All these idealized studies show the impact of the different parts of the barotropic deformation field on baroclinic eddy development and their potentially equal importance; but, because of the complexity of the real jet stream deformation field, its different components have been usually studied separately.

Mak and Cai (1989) offered a simple understanding of the simultaneous action of the stretching and shearing terms without doing any assumption on their form by introducing the deformation vector (the $\vec{D}$ vector) and showing its implication in the barotropic generation term. This simple mathematical formulation is an easy way to study the role of the large-scale deformation on individual cyclone development and have allowed some authors to show the non negligible role played by the barotropic interaction in some real cases (Lackmann et al., 1999; Kucharski and Thorpe, 2000). However, recently, Rivière et al (2003, 2004), hereafter referred respectively to as RHK03 and RHK04, show in a quasigeostrophic context

that the deformation field action cannot be understood by looking only at the $\vec{D}$ vector, as the deformation field has also a rotational component which is reduced to the relative vorticity in its simplest expression. Even if this rotational component is not involved directly in the energy equations, it first acts on the shape of the perturbation (or eddy) and indirectly on the barotropic and baroclinic conversion terms. The aim of the present paper is to interpret the role of the large-scale deformation field on the evolution of observed midlatitude cyclones by using some results developed in RHK03 and RHK04 that take into account the whole deformation tensor and not only a part. Especially, it will be shown that regions where the deformation field is most active do not correspond to large values of the $\vec{D}$ vector modulus but to large values of a diagnostic parameter involving the stretching and shearing terms and the relative vorticity of the large-scale flow, i.e all the horizontal derivatives of the horizontal large-scale wind. Furthermore, as the main interaction for cyclone development is essentially baroclinic (e.g., Ayrault and Joly, 2000), the attempt of the paper is to describe mechanisms showing how the large-scale deformation field modulates baroclinic interaction and especially forces it to occur in some specific regions.

One of the main results of the Fronts and Atlantic Storm-Track EXperiment (FASTEX; Joly et al., 1999) described in Baehr et al. (1999) was that strong deepening rates of cyclones occurred in the eastern Atlantic in a region where the flow is diffluent. Another essential ingredient revealed by this paper is the recurrent 'crossing of the jet stream' from the warm to the cold-air side to get rapid cyclone increase during the FASTEX period. The authors emphasized the fact that these strong deepening rates by crossing the jet occur with or without the presence of a jet streak. The results suggest that these background conditions for rapid cyclone intensification are more related to the large-scale flow spatial structure and occur when the cyclone crosses the large-scale jet in its region of diffluence. The strong cyclone development in the eastern Atlantic seems not to be a specific characterization of the FASTEX period. Young (1995) shows several examples of cyclone development in large-scale

diffluent flows and especially in the eastern Atlantic. Wang and Rogers (2001) studied the different characteristics of cyclones in the Atlantic and showed that the occurrence of strong explosive cyclones in the northeast Atlantic is almost the same than on the northwest side. Moreover, strong explosive cyclone growth can occur in the Atlantic jet-exit region to form devastating wind storms in Europe as it was the case during the christmas storms of 1999. The following paper will focus on the role of the large-scale deformation field on the explosive growth of midlatitude cyclones in the diffluent part of the Atlantic jet stream.

One question that raises naturally from the discussion of the previous paragraph is: how and why do cyclones strongly develop in the diffluent part of the jet in a region where the environmental baroclinicity is not the largest? A natural answer would be to invoke downstream development processes described by Orlanski and Katzfey (1991) and Orlanski and Sheldon (1995). The authors show from case studies evidences that a cyclone can grow by retrieving energy via ageostrophic geopotential fluxes from another cyclone located more upstream which itself grows by extracting energy baroclinically from the mean flow. These processes need more than one synoptic system to occur but some of well-known storms developing at the jet exit were completely isolated from other synoptic systems (this is the case of IOP17 and the christmas storms of december 1999 studied in the paper). Moreover, recent results from Ayrault (1998) and Ayrault and Joly (2000) show that although the strongest growth are not systematically located in regions of largest baroclinicity the main factor responsible for cyclone growth is baroclinic interaction. Furthermore, some authors (Cai and Mak, 1990; Lee and Mak, 1996) showed that the baroclinic generation rate tends to be localized downstream of the baroclinicity maximum. It seems that not much attention has been paid to these results on the location of the baroclinic generation rate, in part because of the emphasis made on redistribution processes and downstream development. However, this peak of the baroclinic generation rate downstream of the baroclinicity maximum will be confirmed in our case studies and will be explained by a mechanism involving the large-scale

deformation field.

Let us note that all the previous cyclone studies on the role of the large-scale deformation were focused either on the initiation stages of surface cyclones or on the development of upper-level precursors; Lackmann et al. (1999) and Kucharski and Thorpe (2000) show how the deformation field can create upper disturbances via barotropic generation terms while Mallet et al. (1999) and Chaboureau and Thorpe (1999) validated the theory proposed by Bishop et Thorpe (1994a,b) on the initiation of new cyclones from frontal wave development. Our study has to be contrasted with those previously cited as it will involve the large-scale deformation field in mature stages of cyclones. The IOP17 cyclone of FASTEX corresponds to one of the strongest cyclones of FASTEX (16-20 february 1997) and is characteristic of the behaviour described by Baehr et al. (1999) as its strongest deepening phase occurred during its second phase of growth in the jet-exit area. While all the previous dynamical studies of IOP 17 have treated the first part of its life cycle (see Mallet et al., 1999a and Arbogast, 2004 for the initial formation of the low-level precursor; see Kucharski and Thorpe, 2000 for the initial formation of the upper-level disturbance; and see Cammas et al., 1999 and Mallet et al., 1999b for the first baroclinic stage of growth and the important role played by the diabatic heating), Part I of the present paper will analyze the dynamical processes involved in the second part of its life cycle from 18 UTC 18 February to 12 UTC 20 February and especially its strong second phase of growth. Part II will deal with the explosive growth of the two christmas storms of 1999 in the eastern Atlantic. The study is decomposed into two parts as IOP17 of FASTEX and the two storms of december 1999 are embedded in two zonal regimes whose deformation fields are very different from each other, as well as the growth mechanisms involved.

In order to study the influence of the large-scale flow on midlatitude cyclones and to use local energetics to confirm our ideas, a simple time filter is used. The flow is thus decomposed into two parts, a high-frequency part corresponding to the cyclone structure

and a low-frequency part associated to the large-scale flow (see Orlanski and Katzfey, 1991; Ayrault, 1998; Lackmann et al., 1999 for a similar decomposition).

The present paper is organized as follows. Section 2 recalls some theoretical results developed in RHK03 and RHK04. Section 3 describes our methodology to adapt this quasi-geostrophic theory to real case studies and recalls also the local energy equations. Section 4 is devoted to the FASTEX reanalysis results during the period 12-28 of february 1997 and especially to the detailed description of the mechanism leading to the last phase of growth of IOP17 in the jet-exit region. A discussion of our results is provided in section 5.

2 Theory of deformation field action in quasigeostrophic flows

All the following analytical results are detailed in RHK03 and RHK04 and are just briefly recalled in the present section. The following perturbation equations are obtained by decomposing the total flow into a reference flow (which satisfies momentum equations and whose quantities are denoted with overbars) and a perturbation (whose quantities are denoted with primes) and by linearizing the momentum equations. The kinetic energy equation within the quasigeostrophic framework can be written as

$$\frac{\bar{D}_g}{Dt}K'_{eg} = \mathbf{E_g}.\mathbf{D_g} - \mathbf{u'_g}.(-\mathbf{k}\times\mathbf{u'_{ag}}),\tag{1}$$

where $\mathbf{u_g}$ and $\mathbf{u_{ag}}$ are respectively the geostrophic and ageostrophic horizontal winds, $K'_{eg} \equiv \mathbf{u'^2_g}/2$ is the perturbation geostrophic kinetic energy, $\bar{D}_g/Dt = \partial/\partial t + \bar{\mathbf{u}}_\mathbf{g}.\nabla$ is the geostrophic lagrangian derivative. The two vectors $\mathbf{E_g}$ and $\mathbf{D_g}$ are defined as

$$\mathbf{E_g} \equiv (\frac{1}{2}(v'^2_g - u'^2_g), -u'_g v'_g),\tag{2}$$

$$\mathbf{D_g} \equiv (\frac{\partial \bar{u}_g}{\partial x} - \frac{\partial \bar{v}_g}{\partial y}, \frac{\partial \bar{v}_g}{\partial x} + \frac{\partial \bar{u}_g}{\partial y}),\tag{3}$$

7

where u_g and v_g are the two components of the geostrophic velocity. $\mathbf{E_g}$ depends on the perturbation anisotropy and $\mathbf{D_g}$ is the deformation vector whose components are the stretching and shearing terms of the reference flow. The scalar product between $\mathbf{E_g}$ and $\mathbf{D_g}$ is the barotropic generation rate and enables the perturbation to extract barotropically energy from the reference flow (see Mak and Cai, 1989). This mathematical formulation yields a simple interpretation; if the angle between $\mathbf{E_g}$ and $\mathbf{D_g}$ is acute, the perturbation extracts energy from the reference flow ($\mathbf{E_g}.\mathbf{D_g} > 0$) whereas if the angle is obtuse, the perturbation loses energy to the reference flow ($\mathbf{E_g}.\mathbf{D_g} < 0$). By noting that the modulus of the $\mathbf{E_g}$ vector is the perturbation kinetic energy ($|\mathbf{E_g}| = K'_{eg}$), and by defining $\bar{\sigma} \equiv |\mathbf{D_g}|$ the modulus of the $\mathbf{D_g}$ vector and ξ' the angle such as $(\widehat{\mathbf{D_g}, \mathbf{E_g}}) \equiv \pi/2 + \xi'$, the barotropic generation rate can be written as

$$\mathbf{E_g}.\mathbf{D_g} = K'_{eg}\bar{\sigma}\sin\xi'. \tag{4}$$

The sign of $\mathbf{E_g}.\mathbf{D_g}$ depends directly on the angle ξ', whose time evolution equation can be derived from the linearized momentum equations under a WKB assumption (see RHK03)

$$\frac{\bar{D}_g\xi'}{Dt} = \bar{\sigma}(r + \cos\xi'). \tag{5}$$

The parameter r has been introduced by Lapeyre et al. (1999) for studying potential vorticity gradient dynamics. It depends solely on the reference flow properties and is defined as

$$r \equiv \frac{\bar{\zeta} + 2\bar{D}_g\bar{\phi}/Dt}{\bar{\sigma}}, \tag{6}$$

where $\bar{\zeta}$ is the basic flow relative vorticity, and $-2\frac{\bar{D}_g\bar{\phi}}{Dt}$ is the rotation rate of the deformation vector $\mathbf{D_g}$ along a Lagrangian path since $(\widehat{\mathbf{Ox}, \mathbf{D_g}}) \equiv \pi/2 - 2\bar{\phi}$ is defined as the angle between the x-axis and the $\mathbf{D_g}$ vector. Let us briefly summarize the results of RHK03 concerning the fixed points of the orientation equation (5). Fixed points of eq.(5) satisfy the property $\frac{\bar{D}_g\xi'}{Dt} = 0$, they are associated with an angle ξ' that will not evolve rapidly along a lagrangian path, i.e correspond to a perturbation structure that is "in equilibrium" with the reference

flow. There are two fixed points in eq (5) which are determined by

$$\xi' = \xi^r_\pm \equiv \pm \arccos(-r), \tag{7}$$

one (ξ^r_-) implies kinetic energy extraction from the reference flow to the perturbation whereas the other (ξ^r_+) leads to loss of perturbation kinetic energy. If ξ' is equal to one of the fixed points, following eq.(4), the exponential barotropic kinetic energy generation rate is equal to

$$\frac{\mathbf{E_g} \cdot \mathbf{D_g}}{K'_{eg}}(\xi' = \xi^r_\pm) = \pm\sqrt{\bar{\sigma}^2 - \left(\bar{\zeta} + 2\frac{\bar{D}\bar{\phi}}{Dt}\right)^2}, \tag{8}$$

and depends only on the reference flow properties.

The contraction (resp. dilatation) axis corresponds to the direction of $\mathbf{u'_g}$ when $\mathbf{E_g}$ is colinear to $\mathbf{D_g}$ (resp. $-\mathbf{D_g}$), i.e when $\xi' = \pi/2$ (resp. $\xi' = -\pi/2$). As the direction of $\mathbf{u'_g}$ with respect to the x-axis forms an angle of $0.5(\xi'-2\bar{\phi})$, we deduce that the angle of the contraction (resp. dilatation) axis with respect to the x-axis is therefore equal to $0.5(-\pi/2 - 2\bar{\phi})$ (resp. $0.5(\pi/2 - 2\bar{\phi})$). The fixed points ξ^r_- and ξ^r_+ define two new axes whose angle with respect to the x-axis are respectively $0.5(-\arccos(-r) - 2\bar{\phi})$ and $0.5(\arccos(-r) - 2\bar{\phi})$ and differ from the dilatation and contraction axes in the general case where $r \neq 0$ (see eq. (7)), i.e when the rotation term $\bar{\zeta} + 2\frac{\bar{D}_g\bar{\phi}}{Dt}$ is non zero. In the notions of dilatation/contraction axes, only the shearing and stretching terms intervene, whereas the deformation field has a rotational component which can modify the orientation of the perturbation anisotropy. This rotational component is taken into account in the term $\bar{\zeta} + 2\frac{\bar{D}_g\bar{\phi}}{Dt}$, i.e in the fixed points formulation of ξ^r_- and ξ^r_+ and indirectly modifies the barotropic generation term (see eq. (8)). In the case where the rotation term $\bar{\zeta} + 2\frac{\bar{D}_g\bar{\phi}}{Dt}$ is larger than the deformation magnitude $\bar{\sigma}$, no fixed points exist as the rotation action is so strong that the perturbation cannot be elongated along a given axis. In other words, in the latter regions, the shape of the perturbation is almost isotropic and barotropic processes are therefore quite weak.

9

3 Methodology

In order to apply the previous quasigeostrophic theory to the FASTEX reanalysis data, it is necessary to decompose the atmospheric flow into two parts, one corresponding to the reference flow and the other to the perturbation. The classical decomposition into a low-frequency part and a high-frequency part that separates the synoptic signal from its environment will be used in all the following results. The temporal filter used is quite simple as the low-frequency field is defined as the time-mean over 8 days of the total field centered on the current date and the high-frequency field is the subtraction of the total field from the low-frequency one. As one week is the typical time scale of a weather regime (Vautard, 1990) and a synoptic signal has usually a period of 2-6 days, a time-mean over 8 days of the total atmospheric flow thus filters the synoptic signal and leads to the flow related to the weather regime. Our study focuses therefore on the interaction between the large-scale flow associated with the weather regime and the synoptic signal. Different tests have shown that the results are not very sensitive to the choice of the filter, once the latter separates the synoptic signal from the large-scale flow. For example, a 6 days or a 10 days time-mean filter leads to the same results as an 8 days one. The form of the filter is not very important either as a Fourier low-pass filter with a given frequency cutoff has been tested and does not change significantly the results shown hereafter. The theory described in the previous section will allow us to better understand the influence of the weather regime or low-frequency flow (denoted hereafter with subscript m) and especially its deformation field on the high-frequency cyclones (denoted hereafter with primes).

3.1 Application of the theory

Remark that the rotation rate of the deformation vector is strong when the reference flow has a strong curvature. This is the case for example when the reference flow is composed of isolated eddies (Lapeyre et al., 1999). But in the present case, the low-frequency flow is

essentially composed of a weakly curved jet stream and the term $2\frac{D_m\phi_m}{Dt}$, which is the rotation rate of the low-frequency deformation vector, can be neglected. Following this remark, the fixed points of eq.(7) can be simplified to

$$\xi_\pm^r \simeq \pm \arccos\left(-\frac{\zeta_m}{\sigma_m}\right), \tag{9}$$

and following expression (8), the following low-frequency diagnostic parameter is introduced

$$\Delta_m \equiv \sigma_m^2 - \zeta_m^2, \tag{10}$$

where ζ_m and σ_m are respectively the relative vorticity and the deformation vector modulus of the low-frequency flow; Δ_m is called hereafter *the effective deformation*. The usual diagnostics to estimate the role of the low-frequency deformation comprise the dilatation/contraction axes (defined as the angle $0.5(\pm\pi/2 - 2\phi_m)$ with respect to the x-axis) and the large values of the deformation magnitude σ_m (Black and Dole, 2000). By contrast, the new parameters suggested by the RHK theory are composed of the fixed points directions (defined as the angle $0.5(\pm \arccos\left(-\frac{\zeta_m}{\sigma_m}\right) - 2\phi_m)$ with respect to the x-axis) and the large values of the effective deformation Δ_m. The additional ingredient is the relative vorticity of the low-frequency flow and the diagnostics take into account all the horizontal inhomogeneities of the low-frequency flow as the stretching, shearing and relative vorticity terms appear in our definitions, i.e all the horizontal derivatives of the horizontal wind. The dynamical role played by regions of positive Δ_m in the cyclone life cycles will be analyzed in the following section and compared to regions of large σ_m.

3.2 Energy budgets

3.2.1 Derivation of the high-frequency eddy kinetic energy equation

The high-frequency eddy kinetic energy equation deduced from the primitive momentum equations in isobaric coordinates can be expressed as

$$\frac{D_m}{Dt}K_e' = -\mathbf{u}'.\nabla_\mathbf{p}.\Phi' - \mathbf{u}'.(\mathbf{u_3'}.\nabla_\mathbf{3}\mathbf{u_m}) + R_1, \tag{11}$$

11

where $K'_e \equiv \mathbf{u'^2}/2$ is the eddy kinetic energy, Φ is the geopotential, $\mathbf{u_3}$ is the three-dimensional velocity vector, $\mathbf{u}$ is the horizontal velocity vector, $\frac{D_m}{Dt} = \frac{\partial}{\partial t} + \mathbf{u_{3m}}.\nabla_\mathbf{3}$ is the three-dimensional lagrangian derivative, $\nabla_\mathbf{p}$ is the horizontal component of the three-dimensional gradient operator in isobaric coordinates ($\nabla_\mathbf{3} = \nabla_\mathbf{p} + \mathbf{k}\partial/\partial p$). The first two terms on the right are respectively the pressure work and the Reynolds stress term. All the other terms are included in the residue term, denoted R_1, which is composed of dissipation, forcing and nonlinear eddy terms (see for more details, Orlanski and Katzfey, 1991).

The pressure work term can be written as the sum of three terms

$$-\mathbf{u'}.\nabla_\mathbf{p}.\Phi' = -\nabla_\mathbf{p}.(\mathbf{u'}\Phi') - \frac{\partial(\omega'\Phi')}{\partial p} - \mathcal{R}\theta'\omega', \tag{12}$$

where $\mathcal{R} \equiv \frac{R}{p}(\frac{p}{p_0})^{\frac{C_v}{C_p}}$, θ is the potential temperature, ω is the vertical velocity in pressure coordinates, R is the gas constant, p_0 is a reference pressure, C_v and C_p are the specific heats of the air, at constant volume and pressure. The first two terms in the right-hand side, $-\nabla_\mathbf{p}.(\mathbf{u'}\Phi')$ and $-\partial(\omega'\Phi')/\partial p$, are respectively the ageostrophic geopotential horizontal and vertical fluxes and redistribute horizontally and vertically eddy kinetic energy. Orlanski and Katzfey (1991) and Orlanski and Sheldon (1995) have shown the crucial role that may play the ageostrophic geopotential horizontal fluxes in the growth of some cyclones. A cyclone can grow essentially by receiving kinetic energy from another one located more upstream which itself has grown by baroclinic interaction: this process is now well-known as downstream development. The third term of eq. (12), $-R\theta'\omega'$, is the baroclinic conversion rate from eddy potential energy to eddy kinetic energy; this term is generally strong when an upper disturbance has a classical baroclinic interaction with a surface one.

The Reynolds stress term can be expressed as follows (see Lackmann et al., 1999)

$$-\mathbf{u'}.(\mathbf{u'_3}.\nabla_\mathbf{3}\mathbf{u_m}) = \mathbf{E}.\mathbf{D_m} - K'_e(\nabla_\mathbf{p}.\mathbf{u_m}) + \omega'(\mathbf{u'}.\frac{\partial \mathbf{u_m}}{\partial p}), \tag{13}$$

where $\mathbf{E} \equiv (\frac{1}{2}(v'^2 - u'^2), -u'v')$ and $\mathbf{D_m} \equiv (\partial u_m/\partial x - \partial v_m/\partial y - v_m \tan\varphi/a, \partial v_m/\partial x + \partial u_m/\partial y + u_m \tan\varphi/a)$. u and v are the two components of the horizontal velocity, φ is

12

latitude, a is the radius of the earth, $\partial/\partial x \equiv (a\cos\varphi)^{-1}\partial/\partial\lambda$ and $\partial/\partial y \equiv a^{-1}\partial/\partial\varphi$ are the horizontal derivatives and λ is longitude. The barotropic generation rate $\mathbf{E}.\mathbf{D_m}$ has been already shown to be important for the appearance of new disturbances in the upper-troposphere (Lackmann et al., 1999; Kucharski and Thorpe, 2001). It is the only term of the Reynolds stress that intervenes in quasigeostrophic dynamics and is usually the predominant term of the Reynolds stress in real case studies.

3.2.2 Derivation of the eddy potential and total energy equations

The eddy potential energy is denoted as $P'_e \equiv \frac{1}{2S}\theta'^2$ with $S \equiv -\mathcal{R}^{-1}(\frac{\partial\theta_0}{\partial p})$ and θ_0 is the potential temperature average at the given level p. The equation governing the eddy potential energy evolution can be expressed as

$$\frac{D_m}{Dt}P'_e = \mathbf{F}.\mathbf{B_c} + \mathcal{R}\omega'\theta' + R_2, \tag{14}$$

where

$$\mathbf{F} \equiv \frac{1}{\sqrt{S}}\theta'(v', -u'), \tag{15}$$

$$\mathbf{B_c} \equiv \frac{1}{\sqrt{S}}(-\frac{\partial\theta_m}{\partial y}, \frac{\partial\theta_m}{\partial x}), \tag{16}$$

and the residue term R_2 contains eddy nonlinear terms, forcing and friction. The baroclinic potential energy generation rate that enables eddies to extract available potential energy from the time-mean flow is written as the scalar product between $\mathbf{F}$ that depends on the perturbation spatial structure and $\mathbf{B_c}$ the baroclinic vector, following the formalism of Cai and Mak (1990). The second term in the right-hand side of eq. (14) is the opposite of the baroclinic conversion rate from eddy potential energy to eddy kinetic energy that appears in the pressure work term (12) and disappears logically in the following total energy equation

$$\frac{D_m}{Dt}T'_e = -\mathbf{u}'.(\mathbf{u'_3}.\nabla_3\mathbf{u_m}) + \mathbf{F}.\mathbf{B_c} - \nabla_\mathbf{p}.(\mathbf{u}'\Phi') - \frac{\partial(\omega'\Phi')}{\partial p} + R_1 + R_2. \tag{17}$$

13

3.3   Optimal instantaneous baroclinic configuration

A simple way to interpret the baroclinic generation term is to divide it by the eddy total energy T'_e and leads to the following expression

$$\frac{\mathbf{F}.\mathbf{B_c}}{T'_e} = |\mathbf{B_c}|.conf = |\mathbf{B_c}|.\frac{\frac{1}{\sqrt{S}}\theta'(v', -u').\mathbf{e_c}}{\frac{1}{2}(u'^2 + v'^2) + \frac{1}{2S}\theta'^2}, \tag{18}$$

where $\mathbf{e_c} \equiv \mathbf{B_c}/|\mathbf{B_c}|$ is the unit vector of the baroclinicity. This new term is called the exponential baroclinic generation rate (see RHK04 for a similar decomposition) as it intervenes in the equation governing the total energy exponential growth rate (see eq.(17)). It is the product of the baroclinicity $|\mathbf{B_c}|$ with a term, hereafter called the configuration term and denoted *conf*, which corresponds to the eddy spatial configuration related to the baroclinicity vector orientation. This configuration term contains two different notions. The first one appears directly from the scalar product expression of the baroclinic generation rate $\mathbf{F}.\mathbf{B_c}$: if the two vectors $\mathbf{F}$ and $\mathbf{B_c}$ are not colinear, i.e if $(\theta'v', -\theta'u')$ is not colinear to $\mathbf{e_c}$, it means that the upper-level disturbance does not align with the surface cyclone along the baroclinicity vector and the whole high-frequency perturbation does not extract optimally the available potential energy from the mean flow. The second idea of configuration is related to the vertical tilt of the perturbation isolines and is much more usual as it is present in the two-dimensional Eady model or in the usual two-layer baroclinic model; it is for example well-known in these simple models that the two waves in the upper and lower-levels must be in phase quadrature for optimum growth (Hoskins et al., 1985; Warrenfeltz and Elsberry, 1989; Davies and Bishop, 1994). This notion can be recovered from the configuration term in the following manner; let us consider a zonal jet and $u' = 0$ (i.e a case where $\mathbf{F}$ is colinear to $\mathbf{B_c}$), then the configuration term is reduced to $\frac{1}{\sqrt{S}}\theta'v'/(\frac{1}{2}v'^2 + \frac{1}{2S}\theta'^2)$ and is optimal for $\frac{1}{\sqrt{S}}\theta' = v'$, which corresponds to a given upward and westward slope of the geopotential isolines as $\theta' \simeq \partial_z\Phi'$ and $v' \simeq \partial_x\Phi'$. This local condition is equivalent to the phase quadrature condition previously described between the upper and lower-level waves. Fig.1 summarizes the two notions of configuration described previously in the context of an upper disturbance interacting with

14

a surface cyclone. Subfigures of Fig.1 presents different configurations leading to a positive baroclinic generation rate, but only one subfigure corresponds to the optimal configuration which is Fig.1.d. The configuration term in Figs.1.a-c is not optimum as in fig.1.a the upper-level disturbance and the lower one do not align with the baroclinicity vector. In Figs.1.b and c, although there is the right alignment, the vertical tilt is not optimal either; in Fig.1.b the geopotential isolines vertical slope is too weak ($\theta' >> v'$), and in Fig.1.c, it is too strong ($\theta' << v'$). Fig.1.d represents the configuration that optimally extracts energy from the mean flow and is equivalent to the phase quadrature condition. It has to be emphasized that the optimality of the baroclinic configurations discussed previously is considered only in the instantaneous sense of the term and no notion of time duration intervenes.

4 FASTEX reanalysis results during the period 12-28 of february 1997

4.1 Dataset

The dataset used is extracted from the 4DVAR reanalysis of FASTEX (Desroziers et al., 2002) and our analysis will focus on the period going from February 12 to February 28 1997. This period corresponds to a well established zonal regime where the horizontal and vertical inhomogeneities of the jet do not change much. We can therefore consider that the large-scale flow acts almost in the same way on all the cyclones of this period. Statistical results during this period are first derived and are followed by a case study of the second stage of growth of IOP17 that occurred from 18 UTC 18 February to 00 UTC 20 February.

4.2 Relation between the low-frequency deformation spatial structure and the high-frequency eddies location

Large values of the square of the low-frequency deformation magnitude, σ_m^2, and of the low-frequency effective deformation Δ_m are respectively plotted in Figs.2.a-b at 00 UTC 19 february 1997. The large difference between the patterns of the two fields proves that the low-frequency relative vorticity reaches values as large as those of the deformation magnitude. The quantity Δ_m has three distinct regions with large positive values along the jet (see Fig.2.b); one located at the jet entrance (hereafter denoted as region 1), another halfway of the jet eastward extent on its anticyclonic (south) side (hereafter denoted as region 2) and the last one at the jet exit on its cyclonic (north) side (hereafter denoted as region 3).[1] Focus first on the jet structure between longitudes 60°W and 20°W; in this region, the deformation magnitude is stronger on the cyclonic side of the jet (see fig.2.a) than on the anticyclonic one whereas the Δ_m field exhibits positive values south of the jet (see fig.2.b) which means that the relative vorticity is strong enough on the cyclonic side compared to the anticyclonic one that Δ_m is negative on the cyclonic side and positive on the anticyclonic one. This result is logical as the jet has globally a slight cyclonic curvature (see the curvature of the wind speed modulus $|\mathbf{u_m}|$ in Figs.2.a-b) leading to large values of vorticity on the northern side of the jet core. It shows also that regions of positive values of Δ_m do not correspond to regions where the horizontal gradients are the strongest. Region 3 located downstream of the jet exit is, by contrast with region 2, characterized by large values of the deformation and is located on the cyclonic side of the jet.

The hatched shadings in Fig.3 represent the high-frequency kinetic energy density at 350 hPa during the period going from February 12 to February 28. The density is defined in appendix and consists in counting at each grid point the number of times the high-

---

[1]The vocabulary "cyclonic" and "anticyclonic" comes from the fact that on the north (resp. south) side of the jet, relative vorticity is negative (resp. positive) (see Thorncroft et al., 1993).

frequency wind speed is above a given threshold (here 40 m.s^{-1}) during this period. In Fig.3.a, we compare the high-frequency kinetic energy density with the low-frequency wind speed modulus at 350 hPa. Between 60°W and 20°W, the high-frequency kinetic energy tends to be essentially located south of the low-frequency speed maximum, i.e in the anticyclonic part of the jet whereas between 20°W and 20°E, it is the opposite, most of the high-frequency kinetic energy is in the cyclonic part of the jet. This figure shows that the high-frequency disturbances tend to cross the jet from the south to the north in the jet-exit region. The superimposition of the high-frequency kinetic energy density upon regions of positive Δ_m (Fig.3.b) shows a very good spatial correspondance between the two quantities; indeed, regions 1, 2 and 3 correspond very well to regions where the high-frequency kinetic energy densities are the largest. In particular, the limit between regions 2 and 3 defined in Fig.2.b, denoted hereafter as BtCR for barotropic critical region, corresponds to a specific region where the high-frequency disturbances tend preferentially to cross the jet. The importance of this region will be emphasized in the following section by studying the last stage of growth of IOP17 of FASTEX. Further note also from Fig.3.b, that downstream of the jet-exit region one part of the large values of the high-frequency densities are located over Scandinavia and another over western Europe and Italy and these two parts are quite well captured by regions of positive Δ_m. Fig.3 shows therefore that the quantity Δ_m is relevant to localize the spatial distribution of the high-frequency disturbances relatively to the jet core which is not the case of the deformation magnitude.

4.3 Last stage of growth of IOP17 at the jet exit

The IOP17 time evolution is essentially decomposed into an initiation stage from 12 UTC 16 February to 12 UTC 17 February, a first growth stage ending at 12 UTC 18 February, a period of decrease until 00 UTC 19 February, a second growth stage ending at about 00 UTC 20 February and finally decreasing. Despite the strong deepening of IOP17 during its

second growth stage, most of the papers on IOP17 have studied its initiation stage or its first growth stage. Mallet et al. (1999a) and Arbogast (2004) have discussed the formation of the new surface cyclone while Kucharski and thorpe (2000) have shown the role played by barotropic processes in the development of the upper-level disturbance that will interact with the surface cyclone. Our study comprises the period of decrease from 12 UTC 18 February to 00 UTC 19 February, the second growth stage and the final decrease and will focus on the dynamical processes leading to the last growth stage in the jet-exit region and that have not been yet studied.

4.3.1 Role of the barotropic critical region

Fig.4 is an overview of the large-scale conditions in which IOP17 is embedded during its second growth stage. The last growth stage occurs in a region located downstream of the low-frequency baroclinicity maximum and during this phase its trajectory goes through the BtCR region. BtCR as already defined in section 4.2 is the limit between two regions of positive values of Δ_m which are located one on the anticyclonic side of the jet and the other on the cyclonic side. BtCR is therefore the bottleneck area between two regions where the dilatation axes are almost perpendicular (see Fig.4) upstream and downstream of it. When IOP17 crosses the jet around BtCR, the low-frequency barotropic environment changes drastically as the dilatation axes change suddenly their orientation. Fig.4 suggests therefore that the barotropic environment may play an important role in the last development of IOP17. Let us mention also that the boundary region of the dilatation axes discontinuity is a line along the jet core that separates the northern side from the southern one. BtCR reduces to almost a point located on this line and this is precisely around this point that IOP17 crosses the jet.

Figs.5 and 6 describe the time evolution of the synoptic system associated with IOP17 from 18 UTC 18 February to 12 UTC 20 February as derived from the time filtered fields.

At 18 UTC 18 February (Fig.5.a), the system of interest (in the lower-left side of the figure) is well developed with an upper-level disturbance interacting baroclinically with the surface cyclone which can be seen from the slight downstream location of the low-level geopotential trough relative to its upper-level counterpart. Remark also another high-frequency system in the upper-right side of the figure. These two systems are on two different sides of the jet, IOP17 is on the anticyclonic side whereas the other one is on the cyclonic one; this is consistent with the fact that IOP17 develops a south-west to north-east tilt whereas the other synoptic system has a south-east to north-west one. 6 hours later (Fig.5.b), the amplitude of the two systems have decreased and their large elongation along the dilatation axes suggests that the decrease is due to a negative barotropic generation rate. This result will be confirmed in the next section from an energy budget analysis. Concerning IOP17, the geopotential associated with the surface cyclone is more stretched than the upper-level disturbance and at 00 UTC 19 february (Fig.5.b), it has two local minima, and that located the most downstream was not present 6 hours earlier. This second deepening downstream of the whole synoptic system is strongly reinforced at 06 UTC 19 February (Fig.5.c) whereas the first one disappears and it is accompanied with a rapid change of the surface cyclone anisotropy. Properties of the surface cyclone dynamics change rapidly from 18 UTC 18 February to 06 UTC 19 February and these changes coincide with the crossing of the jet around BtCR. As it will be shown in the next paragraph, it is related to the discontinuity of the dilatation axes and to the barotropic generation term in the low levels.

At 12 UTC 19 February (Fig.5.d), the surface cyclone is slightly stronger than at 18 UTC 18 February and because of the rapid appearance of the second minimum at 900 hPa downstream of the whole synoptic system, the relative distance between the geopotential minima at 350 hPa and 900hPa increases strongly between 00 UTC 18 February and 12 UTC 19 February. It shows that the tilt with height of the geopotential isolines increases too and suggests that dynamics of the low levels have changed the vertical configuration of the whole

19

synoptic system. The relative position of the high-frequency geopotential troughs in the upper and lower-levels at 18 UTC 19 February (Fig.6.a) seems to be closer to the schematic optimal baroclinic configuration shown in Fig.1.d whereas 6 hours before (Fig.5.d) the configuration resembles more that of Fig.1.b. This new vertical configuration is favourable to a restarting baroclinic interaction between the upper disturbance and the surface cyclone as will be confirmed in the next section. At 00 UTC 20 February (Fig.6.b), the cyclone gains its maximum amplitude and begins to stretch along a SE-NW axis which is more visible at 06 UTC 20 February (Fig.6.c) and at 12 UTC 20 February (Fig.6.d). This strong elongation along the dilatation axis suggests large negative barotropic generation rates and could explain the decrease of the synoptic system after 00 UTC 20 February. Let us finally emphasize that the whole synoptic system associated with IOP17 composed of the upper disturbance and the surface cyclone evolves in regions where Δ_m at 350 hPa is positive suggesting that the horizontal inhomogeneities of the jet acts on the IOP17 trajectory. Note that the field Δ_m is almost barotropic in this case and vertically averaging Δ_m leads to a field similar to Δ_m at 350 hPa. This result on IOP17 trajectory confirms on an example what has already been shown from a statistical point of view in the previous section. To summarize the results of Figs.5 and 6, the last stage of growth of IOP17 seems to be due to a temporary interruption of the barotropic sink as it crosses the jet and to a new favourable baroclinic configuration between the upper disturbance and the surface cyclone. The favourable configuration seems to be initiated by the rapid appearance of a geopotential minimum in the low levels far downstream of the upper-level geopotential minimum. This dynamical description of the second stage of growth of IOP17 will now be quantitatively verified.

Barotropic processes in the low levels between 18 UTC 18 February and 06 UTC 19 February are presented in more details in Fig.7. At 18 UTC 18 February (Fig.7.a), the high-frequency geopotential is entirely located south of the low-level jet, is stretched along the dilatation axes and the barotropic generation term is strongly negative. At 00 UTC 19

20

February (Fig.7.b), one part of the cyclone is located south of the jet where there is still a strong barotropic decrease. The other part is already north of the jet where the geopotential isolines are perpendicular to the dilatation axes and the barotropic generation term is positive. Let us remark that the sum of $\mathbf{E}.\mathbf{D_m}$ and the divergence term $-K'_e(\nabla_{\mathbf{p}}.\mathbf{u_m})$ is plotted because the two terms act in the same way but the essential signal comes from the classical term $\mathbf{E}.\mathbf{D_m}$ (see next section for a quantitative comparison). The barotropic generation term is positive around the second local minimum of geopotential and can therefore explain its appearance at 00 UTC 19 February. Downstream barotropic growth and upstream barotropic decay is also present 6 hours later (Fig.7.c) and reinforce the cyclone deepening in its downstream part. These three figures firstly show that the temporary decrease of the cyclone between 18 UTC 18 February and 00 UTC 19 February due to barotropic decrease is largely stopped when it crosses the low-level jet. Secondly, they show that the downstream appearance of a local minimum of geopotential and its rapid reinforcement can be explained by barotropic generation of kinetic energy.

4.3.2 Energy budget

An energy budget analysis is performed every 6 hours over a control volume made up of a cylinder centered around IOP17. Although energy and conversions values depend on the control volume, their relative magnitudes and signs are rather insensitive to it, provided that the cylinder remains focused on the system of interest. More precisely, each quantity of the following energy budget is first vertically averaged between two isobars and then averaged over a circle centered around IOP17. The center of the circle is precisely the barycenter around IOP17 of the vertically averaged energetic quantity considered.

Fig.8.a represents the time evolution of the vertically averaged (200-900 hPa) high-frequency total energy T'_e from 18 UTC 17 February to 12 UTC 20 February. It decreases from 18 UTC 18 February to 12 UTC 19 February, then increases until 00 UTC 20 Febru-

ary and finally decreases. A first guess to interpret this evolution is given by plotting the time evolution of the baroclinic generation rate and the Reynolds stress term averaged over the same control volume as the total energy (see Fig.8.b). The baroclinic generation term is positive and almost constant from 06 UTC 18 February to 18 UTC 19 February with a last peak occurring at 18 UTC 19 February. The Reynolds stress term is almost negative at each time except at 18 UTC 19 February where it is slightly positive and by contrast with the baroclinic generation term has strong variations; especially it has a large increase from 18 UTC 18 February to 00 UTC 20 February. This large increase corresponds to the crossing of the jet of IOP17 and to the rapid change of the dilatation axes orientation. It does not lead to a significant positive barotropic generation rate (just a very slight positive peak at 18 UTC 19 February) but it stops the barotropic sink which was responsible for the IOP17 weakening between 12 UTC 18 February and 00 UTC 19 February. The total energy generation rate, sum of the two previous generation rates (solid line in Fig.8.b), is negative by 12 UTC 19 February, then positive until 06 UTC 20 February and finally negative after 12 UTC 20 February. Its sign corresponds quite well to variations of total energy and in particular, during the period of total energy increase from 12 UTC 19 February to 00 UTC 20 February, it is positive and has a well-defined peak at 18 UTC 19 February. Even though redistribution terms were not analyzed here, information given by the signs of the generation rates is enough to explain the time evolution of the total energy associated with IOP17.

An energy budget analysis is performed in Fig.9 for the vertically averaged (200-900 hPa) high-frequency kinetic energy K'_e from 18 UTC 17 February to 12 UTC 20 February. Its time evolution is plotted in Fig.9.a and has almost the same variations as T'_e previously discussed in Fig.8.a, apart from short time intervals. It has in particular a significant increase between 12 UTC 19 February and 00 UTC 20 February as well as T'_e. The time evolution of the pressure work and the Reynolds stress term, as well as their sum which are the main terms intervening in the right-side of eq. (11) are plotted in Fig.9.b. The sum has a well defined

positive peak at 18 UTC 19 February that remarkably fits kinetic energy increase between 12 UTC 19 February and 00 UTC 20 February. Similarly to the conclusion of Fig.8, this positive peak is essentially due to the interruption of the barotropic decrease and to the significant positive sign of the pressure work although the latter has a slight decrease since 00 UTC 19 February. The pressure work is the sum of three terms (see eq.(12)) whose time evolutions are shown in Fig.9.c. The baroclinic conversion term (dotted line with diamonds in Fig.9.c) is always positive, is almost constant from 06 UTC 18 February to 18 UTC 19 February and follows approximately the time evolution of the baroclinic generation term (dotted line with diamonds in Fig.8.b). The sign of the term related to the ageostrophic geopotential horizontal fluxes is anti correlated with the kinetic energy variations as it is positive when kinetic energy decreases (between 00 UTC 18 February and 06 UTC 19 February) and is slightly negative at 18 UTC 19 February during the largest increase of kinetic energy. This anticorrelation is logical as this term is the dispersion term of kinetic energy; if kinetic energy increases, the term is negative around the region of increase and acts to redistribute energy from the source region to other regions; the opposite occurs if there is kinetic energy decrease. This term could be however dynamically important (see e.g., Orlanski and Katzfey, 1991) as it may redistribute energy from a growing cyclone to another one located downstream of it. But the IOP17 is isolated from other cyclones, and thus cannot receive energy from another cyclone via ageostrophic geopotential horizontal fluxes. The ageostrophic geopotential vertical flux is always negative as it acts to disperse energy above the level 200hPa and below 900hPa. From Fig.9, we conclude that the positive sign of the pressure work is due to baroclinic conversion from eddy potential energy to eddy kinetic energy. Analysis of the Reynolds stress term is presented in Fig.9.d, and shows clearly that most of its variations are due to the barotropic generation term $\mathbf{E}.\mathbf{D_m}$. The divergence term is completely negligible while the vertical term $\omega'(\mathbf{u}'.\frac{\partial \mathbf{u_m}}{\partial p})$ has a significant peak at 18 UTC 19 February but is not very important compared with $\mathbf{E}.\mathbf{D_m}$.

The same analysis as in Fig.9 is shown in Fig.10 but for the evolution of kinetic energy in the low levels (600-900hPa). This, in principle, focuses better on the low-level cyclone. Kinetic energy in the low levels (Fig.10.a) has two maxima at 06 UTC 18 February and at 18 UTC 19 February whose amplitudes are comparable to each other and it was not the case for the averaged kinetic energy over the entire troposphere (Fig.9.a). The second growth stage of IOP17 in the low levels is almost as strong as the first one. The sign of the sum of the pressure work and the Reynolds stress (solid line with circles in Fig.10.b) is quite well correlated in time with the variations of kinetic energy (Fig.10.a), even better than it was in Fig.9. The peak at 18 UTC 19 February of the sum of the two terms corresponds to both a peak of the Reynolds term and the pressure work even though the positive sign is due essentially to the latter. The analysis of the pressure work in Fig.10.c firstly shows as in Fig.9.c, that the ageostrophic geopotential horizontal flux does not play at all a role in the peak of the pressure work and acts to disperse kinetic energy. However, a large difference has to be made between Fig.10.c and Fig.9.c with the ageostrophic geopotential vertical flux; this term has a large increase between 12 UTC 18 February and 00 UTC 20 February in Fig.10.c which is not present in Fig.9.c. It means that a large part of kinetic energy created in the upper levels tend to be vertically redistributed downward in the low levels. It has to be noticed that this particular point on vertical redistribution of energy cannot be explained by invoking the theory described in sections 2 and 3 but it has to be taken into account to understand the particular strong development of the surface cyclone. This behaviour added to the significant positive baroclinic conversion rate between 06 UTC 18 February and 18 UTC 19 February is responsible for the peak of the pressure work at 18 UTC 19 February. Concerning the Reynolds stress term (Fig.10.d), its behaviour is very similar to Fig.9.d, and the main term is still the barotropic generation rate.

The energy budget analysis depicted in Figs.8, 9 and 10 agree with the description of section 4.3.1. The second growth stage is due to an interruption of the barotropic sink

during the crossing of the jet and to significant positive baroclinic conversion rates until 18 UTC 19 February, i.e to the maintenance of the baroclinic interaction between the upper disturbance and the surface cyclone far downstream of the baroclinicity maximum. Note that although the analysis of the conversion and redistribution energy terms does not allow to recover exactly energy growth rates, as forcing, dissipation and diabatic terms that may be important have been neglected, it is enough to understand the time variations of the IOP17 energy and the dynamical processes responsible for these variations.

Now the baroclinic generation rate is analyzed by quantifying the different terms of eq.(18) more precisely. The time evolution of the baroclinic generation rate in Fig.11 (solid line with diamonds) has been already shown in Fig.8.b (dotted line with diamonds) and has essentially two local peaks, one at 06 UTC 18 February, and the second at 18 UTC 19 February which has approximately two-thirds of the amplitude of the first one. At 06 UTC 18 February, the cyclone is in its first growth stage located around the maximum speed of the low-frequency jet. It evolves in a baroclinic environment approximately 1.5 times larger than at 18 UTC 19 February during the second growth stage (see dash-dotted line). But the term $\mathbf{F}.\mathbf{B_c}/T_e' = |\mathbf{B_c}|.conf$ composed of the multiplication of the baroclinicity by the configuration term has a well defined peak at that later time and is almost 1.5 times weaker at the time of the first peak which means that the configuration term is more than twice larger at 18 UTC 19 February than at 06 UTC 18 February. Furthermore, due to the barotropic sink, total energy has diminished by a factor of 2 between 06 UTC 18 February and 18 UTC 19 February. The large increase of the configuration term makes up in part the decrease of both the baroclinicity and the total energy to such an extent that the amplitude of the peak of the baroclinic generation rate at 18 UTC 19 February is just two-thirds (times) that of the peak at 06 UTC 18 February, whereas it would be significantly weaker if there was no increase of the configuration term. Fig.11 underlines the large difference in dynamical processes of the two growth stages of IOP17.

Fig.12 exhibits the same idea but from a spatial point of view as the pattern associated with the baroclinic generation rate (Fig.12.a) bears a close resemblance at 18 UTC 19 February with that of $|\mathbf{B_c}|.conf$ (Fig.12.b) and not at all with that of the baroclinicity $|\mathbf{B_c}|$. The strong similarity between $\mathbf{F.B_c}$ and $|\mathbf{B_c}|.conf$ shows that the peak of the baroclinic generation rate is essentially due to the configuration term and not at all due to the baroclinicity. It is interesting to note that the location of the baroclinic generation rate and most of its spatial pattern can be recovered from the quantity $\mathbf{F.B_c}/T_e' = |\mathbf{B_c}|.conf$ where no notion of high-frequency amplitude is introduced, only the environmental baroclinicity and the configuration term intervenes.

5 Discussion

A new diagnostic parameter, called effective deformation and denoted Δ_m, has been introduced in this study following the quasigeostrophic theory of RHK03 and RHK04 and has been shown to be relevant to analyze the role played by the horizontal inhomogeneities of the large-scale flow in the development of midlatitude cyclones. Regions in the upper-troposphere where the low-frequency criterion $\Delta_m > 0$ is satisfied, i.e where the low-frequency deformation magnitude is greater than the absolute value of the low-frequency relative vorticity are shown to coincide with the localization of the high-frequency disturbances. In other words, these regions deduced from the horizontal inhomogeneities of the low-frequency upper-tropospheric jet corresponds to regions where the synoptic perturbations tend to propagate. From the knowledge of this criterion, one is able to deduce at each longitude on which side of the jet (cyclonic or anticyclonic) synoptic eddies tend to be located. As it has been emphasized, this preferred side is changing when moving along the jet. Note that this behaviour has been confirmed by analyzing different types of jet and weather regimes, such as the other example to be given in part II.

More precisely, the two-dimensional map determined by the criterion $\Delta_m > 0$ presents

distinct large-scale regions inside which the dilatation axes have almost the same orientation. On the other hand, the transition from one such large-scale region to the next which is usually almost reduced to a contact point is characterized by a sudden change of the dilatation axes orientation. For example, in the jet-exit region of mid-february 1997, there is a contact point between two regions of $\Delta_m > 0$, one located upstream on the anticyclonic side and another downstream on the cyclonic one where the dilatation axes change suddenly their orientation. This contact point, called barotropic critical region in the text, has been shown to be the preferred region where synoptic eddies tend to cross the jet from the south to the north and is a specific place where barotropic development has very good chance to occur. It was in particular the case for IOP17 whose scenario can be summarized as follows; during its travel on the anticyclonic side, the high-frequency eddy develops a strong south-west to north-east tilt, indicating a strong elongation along the dilatation axes and hence a large barotropic decrease but as it is crossing the barotropic critical region, the eddy is rapidly reshaped and go through a stage of barotropic growth or at least there is an interruption of the barotropic sink. This barotropic process explains the fact that the large weakening of IOP17 is stopped at 00 UTC 19 February and is one of the cause leading to the second growth stage of IOP17 after this date. Note that a similar contact point exists also in the jet-entrance region, suggesting that barotropic activity may be important in this part of the jet too.

The original idea for such a barotropic process comes from the theoretical study of Farrell (1989), where it is shown that a perturbation embedded in a confluent flow will be stretched zonally and will be compacted in the diffluent flow region leading to perturbation kinetic energy growth. This barotropic process has been already proved to be important in real cases for the formation and maintenance of disturbances in the upper-troposphere (Lackmann et al., 1999; Kucharski and Thorpe, 2000) but is here shown to take place also at the low levels and not to call on a wave instability mechanism. Furthermore, our approach predicts

from the large-scale flow alone the regions where such dynamics are likely to occur; these are the barotropic critical regions defined by the low-frequency quantity Δ_m. It should be emphasized that such a critical region cannot be reduced to the mere separation between a confluent and a diffluent region. Indeed, for the zonal regime studied, two critical regions are simultaneously present over the Atlantic jet and not simply one. The definition proposed takes into account the complex actual deformation field.

Another new point provided by this study is the description of the barotropic processes in the low levels that can lead to a new favourable configuration for baroclinic interaction between the surface cyclone and the upper-level disturbance. During the crossing of the jet, the surface cyclone deepens rapidly downstream of its initial quasi vertical structure due to positive barotropic generation of kinetic energy. This increases the distance between the high-frequency geopotential minima at the upper and lower-levels and therefore the tilt with height of the high-frequency geopotential isolines. Despite the weakening of baroclinicity in the jet-exit region, this new favourable configuration allows the baroclinic generation rate to remain constant and even to present a slight peak when the cyclone reaches the British Isles, i.e far downstream of the baroclinicity maximum. The mechanism just described shows how barotropic processes can modify the baroclinic interaction between a surface cyclone and an upper-level disturbance, it provides a rationale for the FASTEX cyclones strengthening during their crossing of the jet in the jet-exit region as described by Baehr et al. (1999) and could be an important mechanism to explain the growth of cyclones in the eastern Atlantic ocean and over western Europe. Part II of the present paper will however present why the details of this process does not apply to all cases and that the notion of "crossing of the jet" hides a variety of mechanisms depending on the spatial structure of the deformation field of the low-frequency jet.

Appendix: Density function

In the present appendix, the algorithm leading to the high-frequency kinetic energy density of Fig.3 is described. The density function $D(x,y)$ is first initialized to zero. At each time step during the period of interest, and at each grid point (x_0, y_0) satisfying the threshold condition $|\mathbf{u}'|(x_0, y_0) > 40$ m.s^{-1}, we consider all its neighbouring grid points (x,y) (those belonging to a circle centered in (x_0, y_0) whose diameter corresponds to 4 degree in latitude) satisfying also the threshold condition $|\mathbf{u}'|(x,y) > 40$ m.s^{-1}, and the density function for these particular grid points is incremented by $D(x,y) = D(x,y) + 1$. Such a definition of the density function $D(x,y)$ gives a stronger weight to grid points surrounded by other ones satisfying also the threshold condition. It leads to smoother contours than if we have used the simple definition that consists to count the number of times during the period of interest that each grid point satisfies the threshold condition but does not change the results.

References

Arbogast, P. 2004. Frontal wave development by interaction between a front and a cyclone: Application to the FASTEX IOP 17. *Quart. J. Roy. Meteor. Soc.*, **130**, 1675-1696.

Ayrault, F. 1998. 'Environnement, structure et évolution des dépressions météorologiques: réalité climatologique et modèles types'. PhD thesis, université P. Sabatier, Toulouse.

Ayrault, F. and Joly, A. 2000. Une nouvelle typologie des dépressions météorologiques: classification des phases de maturation. *C. R. Acad. Sci. Paris, Sciences de la terre et des planètes/ Earth and Planetary Sciences,* **330**, 167-172.

Baehr, C., Pouponneau, B., Ayrault, F. and Joly, A. 1999. Dynamical characterization of the FASTEX cyclogenesis cases. *Quart. J. Roy. Meteor. Soc.*, **125**, 3469-3494.

Barcilon, A. and Bishop, C. H. 1998. Nonmodal development of baroclinic waves undergoing

horizontal shear deformation. *J. Atmos. Sci.*, **55**, 3583-3597.

Bishop, C. H. 1993. On the behavior of baroclinic waves undergoing horizontal deformation. I: The 'RT' phase diagram. *Quart. J. Roy. Meteor. Soc.*, **119**, 221-240.

Bishop, C. H. and Thorpe, A. J. 1994a. Frontal wave stability during moist deformation cyclogenesis. I: Linear wave dynamics. *J. Atmos. Sci.*, **51**, 852-873.

Bishop, C. H. and Thorpe, A. J. 1994b. Frontal wave stability during moist deformation cyclogenesis. II: The suppression of non-linear wave development. *J. Atmos. Sci.*, **51**, 874-888.

Black, R. X. and Dole, R. M. 2000. Storm tracks and barotropic deformation in climate models. *J. of Climate*, **13**, 2712-2728.

Cai, M. and Mak, M. 1990. On the basic dynamics of regional cyclogenesis. *J. Atmos. Sci.*, **47,** 1417-1442.

Cammas, J.P., Pouponneau, B., Desroziers, G., Santurette, P., Joly, A., Arbogast, P., Mallet, I., Caniaux, G., and Mascart, P. 1999. FASTEX IOP17 cyclone: Introductory synoptic study with field data. *Quart. J. Roy. Meteor. Soc.*, **125**, 3393-3414.

Chaboureau, J. P. and Thorpe, A. J. 1999. Frontogenesis and the development of secondary wave cyclones in FASTEX. *Quart. J. Roy. Meteor. Soc.*, **125**, 925-940.

Davies, H. C., Schar, C. and Wernli, H. 1991. The palette of fronts and cyclones within a baroclinic wave-development. *J. Atmos. Sci.*, **48**, 1666-1689.

Davies, H. C., and Bishop, C. H. 1994. Eady edge waves and rapid development. *J. Atmos. Sci.*, **51**, 1930-1946.

Desroziers, G., Hello, G. and Thepaut, J-N. 2003. Four-dimensional reanalyses of FASTEX. *Quart. J. Roy. Meteor. Soc.*, **129**, 1301-1315.

Evans, M. S., Keyser, D., Bosart, L. F. and Lackmann, G. M. 1994. A satellite-derived classification scheme for rapid maritime cyclogenesis. *Mon. Wea. Rev.*, **122**, 1381-1416.

Farrell, B. F. 1989. Transient development in confluent and diffluent flow. *J. Atmos. Sci.,* **46**, 3279-3288.

Hoskins, B. J. and West, N. V. 1979. Baroclinic waves and frontogenesis. Part II: Uniform potential vorticity jet flows- cold and warm fronts. *J. Atmos. Sci.,* **36**, 1663-1680.

Hoskins, B. J., McIntyre, M. E. and Robertson, A. W. 1985. On the use and significance of isentropic potential vorticity maps. *Quart. J. Roy. Meteor. Soc.*, **111**, 877-946.

James, I. N. 1987. Suppression of baroclinic instability in horizontally sheared flows. *J. Atmos. Sci.,* **44**, 3710-3720.

Joly, A. and coauthors. 1999. Overview of the field phase of the Fronts and Atlantic Storm-Track EXperiment (FASTEX) project.*Quart. J. Roy. Meteor. Soc.*, **125**, 3131-3163.

Kucharski, F., and Thorpe, A. J. 2000. Upper-level barotropic growth as a precursor to cyclogenesis during FASTEX. *Quart. J. Roy. Meteor. Soc.*, **126**, 3219-3232.

Lackmann, G. M., Keyser, D. and Bosart, L. F. 1999. Energetics of an intensifying jet streak during the experiment on rapidly intensifying cyclones over the Atlantic (ERICA). *Mon. Wea. Rev.,* **127**, 2777-2795.

Lapeyre, G., P. Klein, and Hua, B. L. 1999. Does the traceur gradient vector align with the strain eigenvectors in 2D turbulence. *Phys. Fluids A,* **11**, 3729-3737.

Lau, N.-C. 1988. Variability of the observed midlatitude storm tracks in relation to low-frequency changes in the circulation pattern. *J. atmos. Sci.,,* **45**, 2718-2743.

Lee, W.-J., and Mak, M. 1996. The role of orography in the dynamics of Storm Tracks. *J. Atmos. Sci.,* **53**, 1737-1750.

Mak M. and Cai, M. 1989. Local barotropic instability. *J. Atmos. Sci.*, **46**, 3289-3311.

Mallet, I., Arbogast, P., Baehr, C., Cammas, J.P., and Mascart, P. 1999. Effects of a low-level precursor and frontal stability on cyclogenesis during FASTEX IOP17. *Quart. J. Roy. Meteor. Soc.*, **125**, 3415-3437.

Mallet, I., Cammas, J.P., Mascart, P., and Bechtold, P. 1999. Effects of cloud diabatic heating on the early development of the FASTEX IOP17 cyclone. *Quart. J. Roy. Meteor. Soc.*, **125**, 3439-3467.

Orlanski, I. and Katzfey, J. 1991. The life cycle of a cyclone wave in the Southern Hemisphere. Part I: Eddy energy budget. *J. Atmos. Sci.*, **48**, 1972-1998.

Orlanski, I. and Sheldon J. P. 1995. Stages in the energetics of baroclinic systems. *Tellus*, **47A**, 605-628.

Pierrehumbert, R. T. 1984. Local and global instability of zonally varying flow. *J. Atmos. Sci.*, **40**, 2141-2162.

Rivière, G., Hua B. L. and Klein, P. 2003. Perturbation growth in terms of barotropic alignment properties. *Quart. J. Roy. Meteor. Soc.*, **129**, 2613-2635.

Rivière, G., Hua B. L. and Klein, P. 2004. Perturbation growth in terms of baroclinic alignment properties. *Quart. J. Roy. Meteor. Soc.*, **130**, 1655-1673.

Schultz, D. M., Keyser, D. and Bosart, L. F. 1998. The effect of large-scale flow on low-level frontal structure and evolution in midlatitudes cyclones. *Mon. Wea. Rev.*, **126**, 1767-1791.

Shutts, G. J. 1983. The propagation of eddies in diffluent jet streams: eddy vorticity forcing of "blocking" flow fields. *Quart. J. Roy. Meteor. Soc.*, **109**, 737-761.

Sickmoller, M., Blender, R. and Fraedrich, K. 2000. Observed winter cyclone tracks in the

northern hemisphere in re-analysed ECMWF data. *Quart. J. Roy. Meteor. Soc.*, **126**, 591-620.

Simmons, A. J. and Hoskins, B. J. 1980. Barotropic influences on the growth and decay of baroclinic waves. *J. Atmos. Sci.,* **37,** 1679-1684.

Thorncroft, C. D., Hoskins, B. J. and McIntyre, M. E. 1993. Two paradigms of baroclinic-wave life-cycle behavior. *Quart. J. Roy. Meteor. Soc.*, **119**, 17-55.

Vautard, R. 1990. Multiple weather regimes over the north atlantic: Analysis of precursors and successors. *Mon. Wea. Rev.,* **118**, 2056-2081.

Young, M. V. 1995. Types of cyclogenesis. *Images in Weather Forecasting.* Bader M. J., Forbes G. S., Grant J. R., Lilley R. B. E. and Waters, A. J. Eds., Cambridge University Press, 213-286.

Whitaker, J. S. and Barcilon, A. 1992. Type B Cyclogenesis in a Zonally Varying Flow. *J. Atmos. Sci.,* **49**, 1877-1892.

Wang, C-C and Rogers, J. C. 2001. A composite study of explosive cyclogenesis in different sectors of the north atlantic. Part I: Cyclone structure and evolution. *Mon. Wea. Rev.*, **129**, 1481-1499.

Warrenfeltz, L.L., and Elsberry, R. L. 1989. Superposition effects in rapid cyclogenesis - Linear model studies. *J. Atmos. Sci.,* **46**, 789-802.

List of Figures

Figure 1: Sketch summarizing the optimal configuration for total energy growth through baroclinic interaction. Solid and dash black lines correspond respectively to upper and lower-level disturbances. The gray and black arrows represent respectively the baroclinicity vector $\mathbf{B_c}$ and the perturbation vector $\mathbf{F}$. In all subfigures, the baroclinic generation rate is positive but the baroclinic configuration is in (a) non optimal as $\mathbf{B_c}$ and $\mathbf{F}$ are not colinear, (b) non optimal as $\theta' >> v'$ even if $\mathbf{B_c}$ and $\mathbf{F}$ are colinear, (c) non optimal as $\theta' << v'$ even if $\mathbf{B_c}$ and $\mathbf{F}$ are colinear, and (d) optimal as $\mathbf{B_c}$ and $\mathbf{F}$ are colinear and $\theta' \simeq v'$.
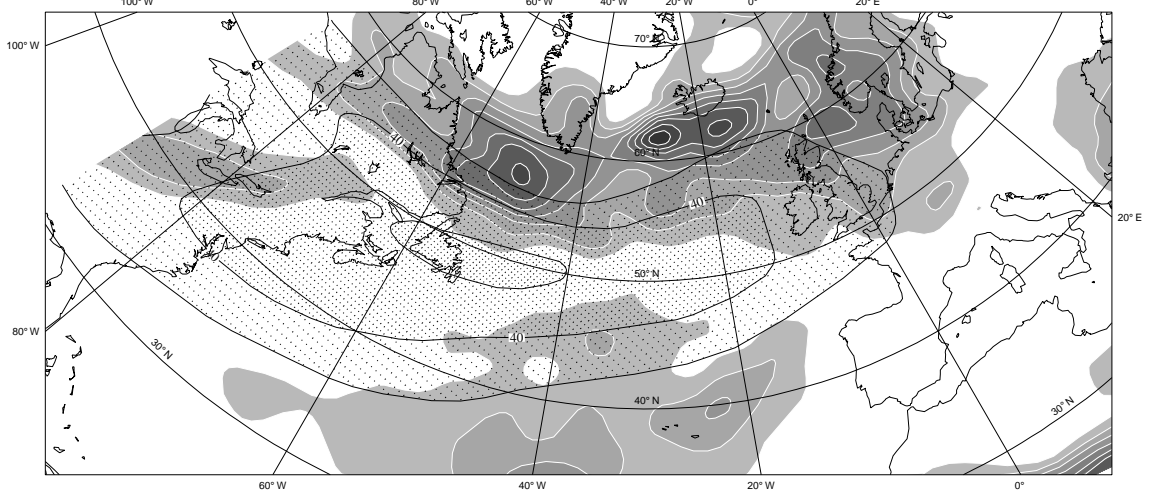
(a)
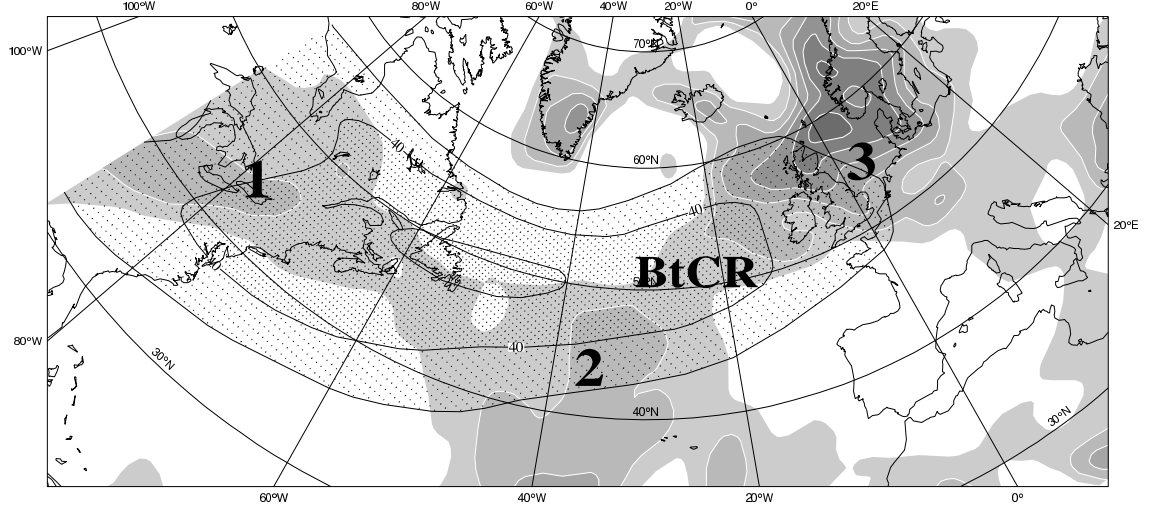
(b)

Figure 2: Wind speed $|\mathbf{u_m}|$ larger than 30 m.s^{-1} at 350 hPa (dotted shadings and contours, interval 10 m.s^{-1}) with (a) the square of the deformation vector modulus σ_m^2 larger than 5.10^{-10} s^{-2} (shaded contours, interval 5.10^{-10} s^{-2}) and (b) positive values of the low-frequency effective deformation Δ_m (shaded contours, interval 5.10^{-10} s^{-2}).
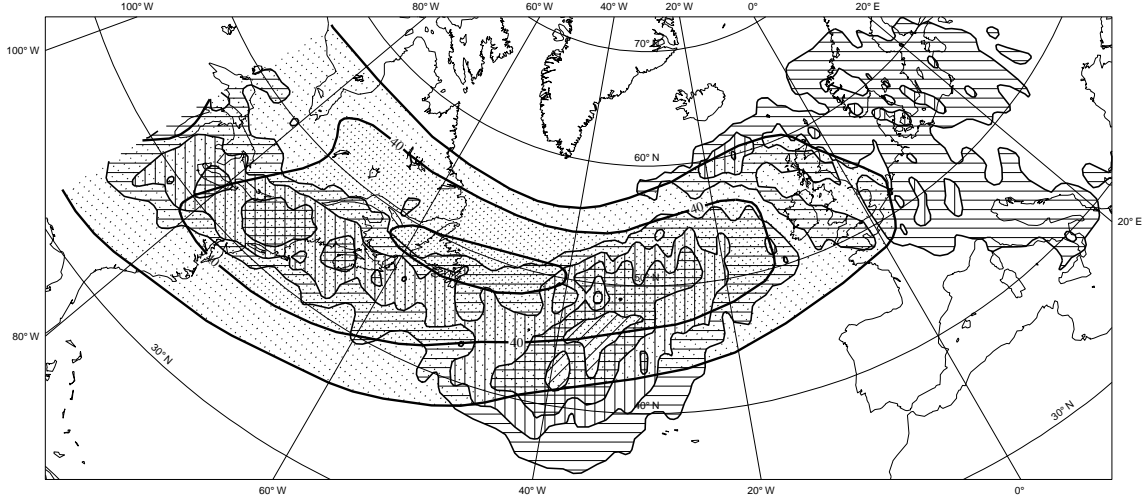
(a)
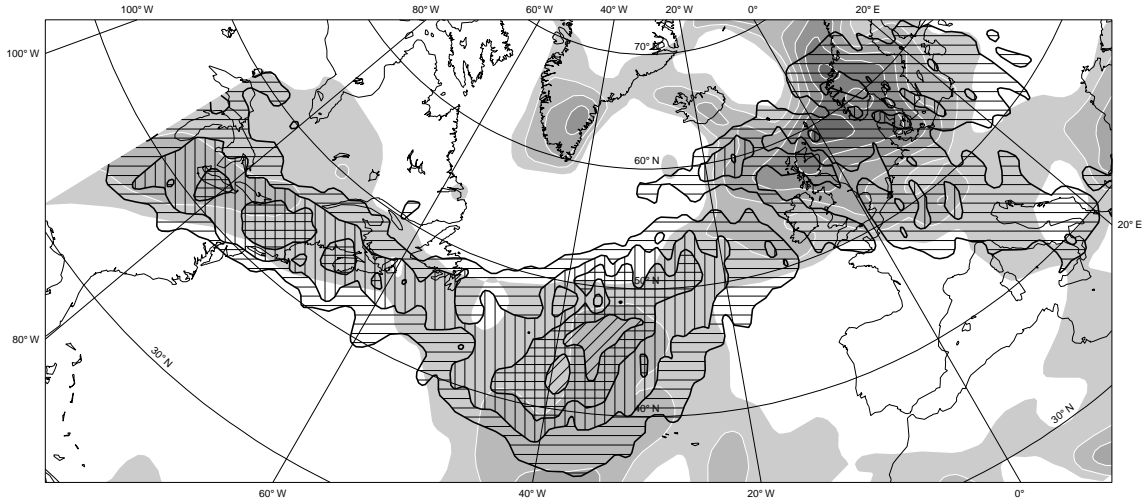
(b)

Figure 3: High-frequency kinetic energy density at 350 hPa during the period 12-28 february 1997 (number of times for which $|\mathbf{u'}| > 40$ m.s^{-1} at each grid point, hatched shadings) with (a) the wind speed $|\mathbf{u_m}|$ larger than 30 m.s^{-1} (dotted shadings and black contours, interval 10 m.s^{-1}) and (b) the positive values of the low-frequency effective deformation Δ_m (shaded, white contours, interval 5.10^{-10} s^{-2}).
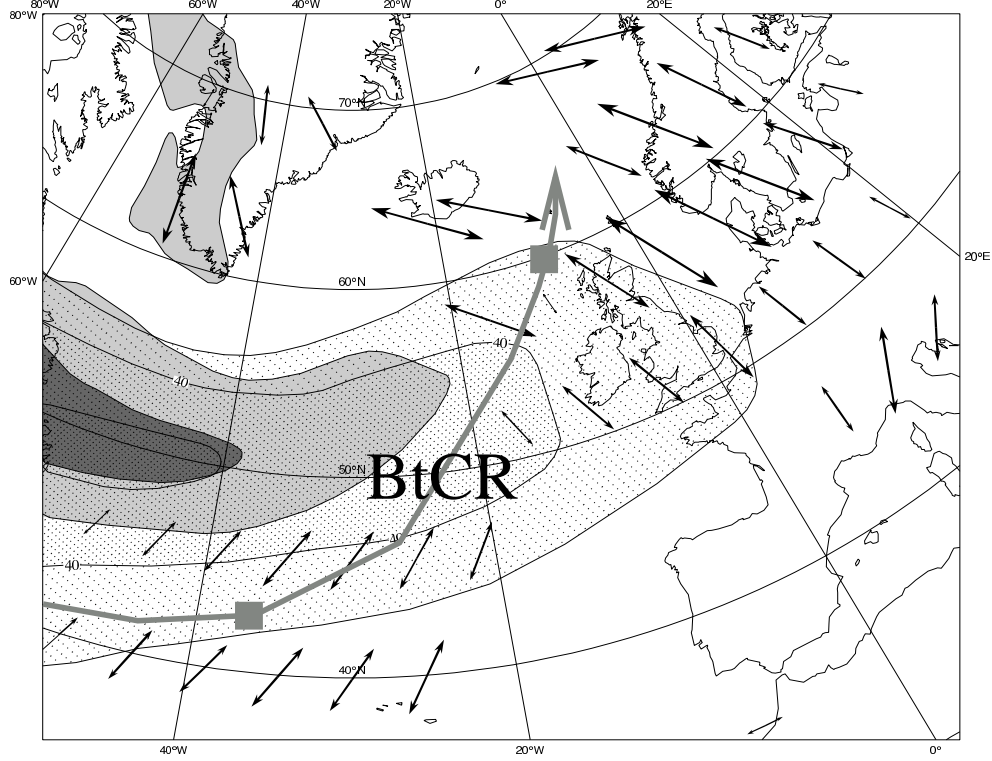
Figure 4: Trajectory of IOP17 of FASTEX in the jet-exit region (large gray arrow), its positions at the beginning (18 UTC 18 February) and at the end (00 UTC 20 February) of its last growth stage (gray squares). Vertically averaged (900-200hPa) low-frequency baroclinicity $|\mathbf{B_c}|$ larger than 3.10^{-5} s^{-1} (shaded contours, interval 10^{-5} s^{-1}), wind speed $|\mathbf{u_m}|$ larger than 30 m.s^{-1} (dotted shadings and light black contours, interval 10 m.s^{-1}) and vertically averaged dilatation axes (black double arrows) in regions where the vertically averaged effective deformation Δ_m is positive at 00 UTC 19 February.
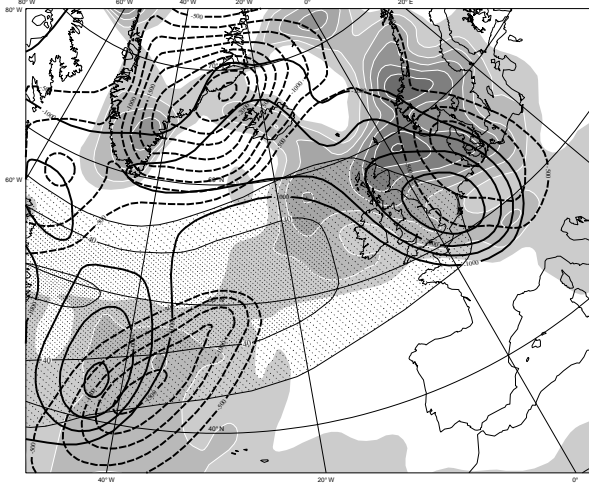
(a) 18 UTC 18 Feb
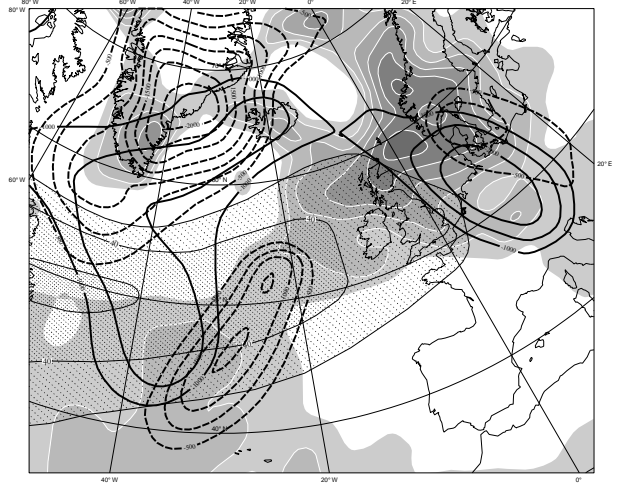
(b) 00 UTC 19 Feb
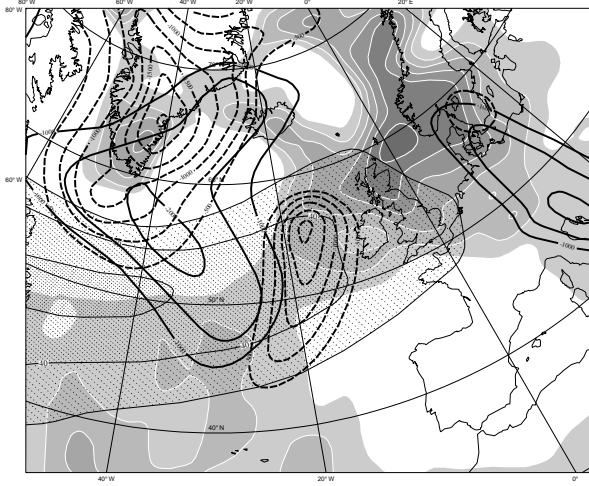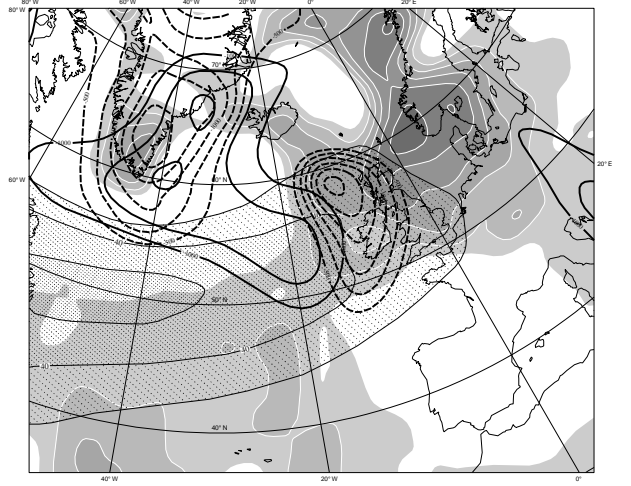
(c) 06 UTC 19 Feb

(d) 12 UTC 19 Feb

Figure 5: Low-frequency wind speed $|\mathbf{u_m}|$ at 350 hPa larger than 30 m.s^{-1} (dotted shadings and light contours, interval 10 m.s^{-1}), positive values of the low-frequency effective deformation Δ_m at 350 hPa (shaded, white contours, interval 5.10^{-10}s^{-2}), high-frequency geopotential at 350 hPa smaller than -500 m^{2}s^{-2} (thick solid contours, interval 500 m^{2}s^{-2}) and high-frequency geopotential at 900 hPa smaller than -250 m^{2}s^{-2} (thick dashed contours, interval 250 m^{2}s^{-2}): (a) 18 UTC 18 Feb, (b) 00 UTC 19 Feb, (c) 06 UTC 19 Feb and (d) 12 UTC 19 Feb.
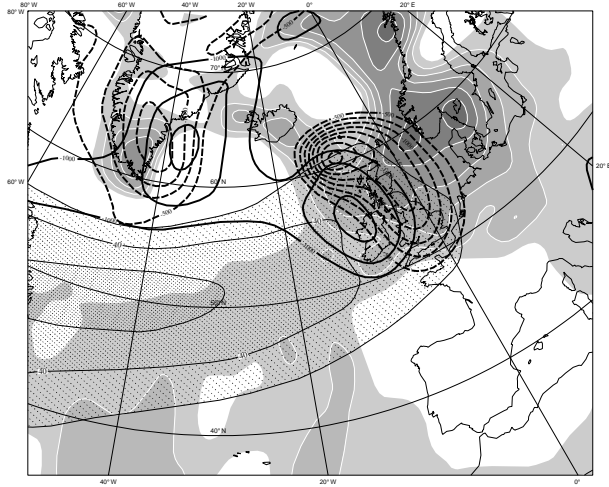
(a) 18 UTC 19 Feb
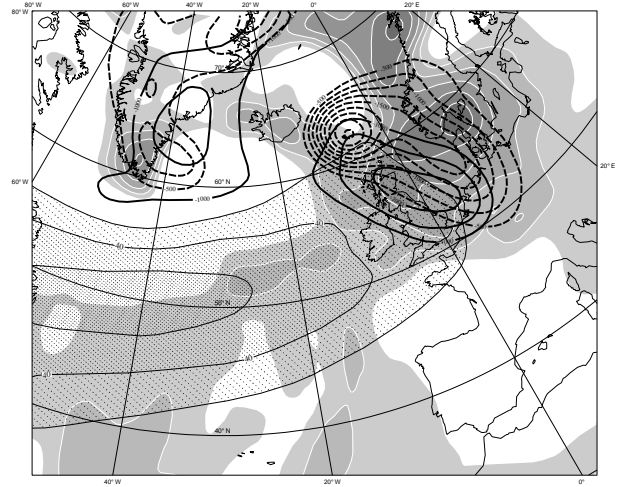
(b) 00 UTC 20 Feb
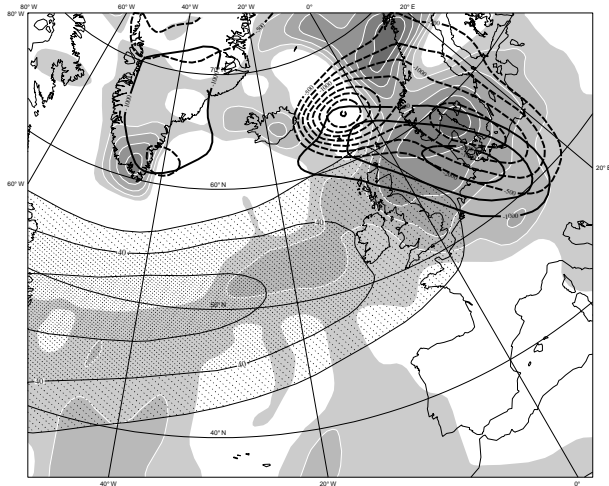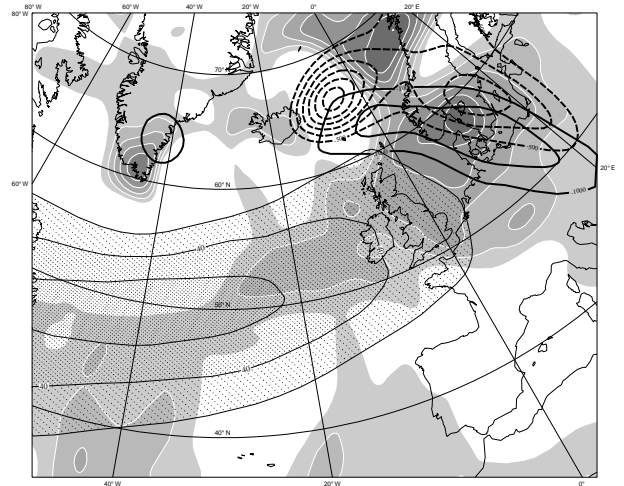
(c) 06 UTC 20 Feb

(d) 12 UTC 20 Feb

Figure 6: Same as in Fig.5, but for (a) 18 UTC 19 Feb, (b) 00 UTC 20 Feb, (c) 06 UTC 20 Feb and (d) 12 UTC 20 Feb.

(a) 18 UTC 18 Feb

(b) 00 UTC 19 Feb

(c) 06 UTC 19 Feb
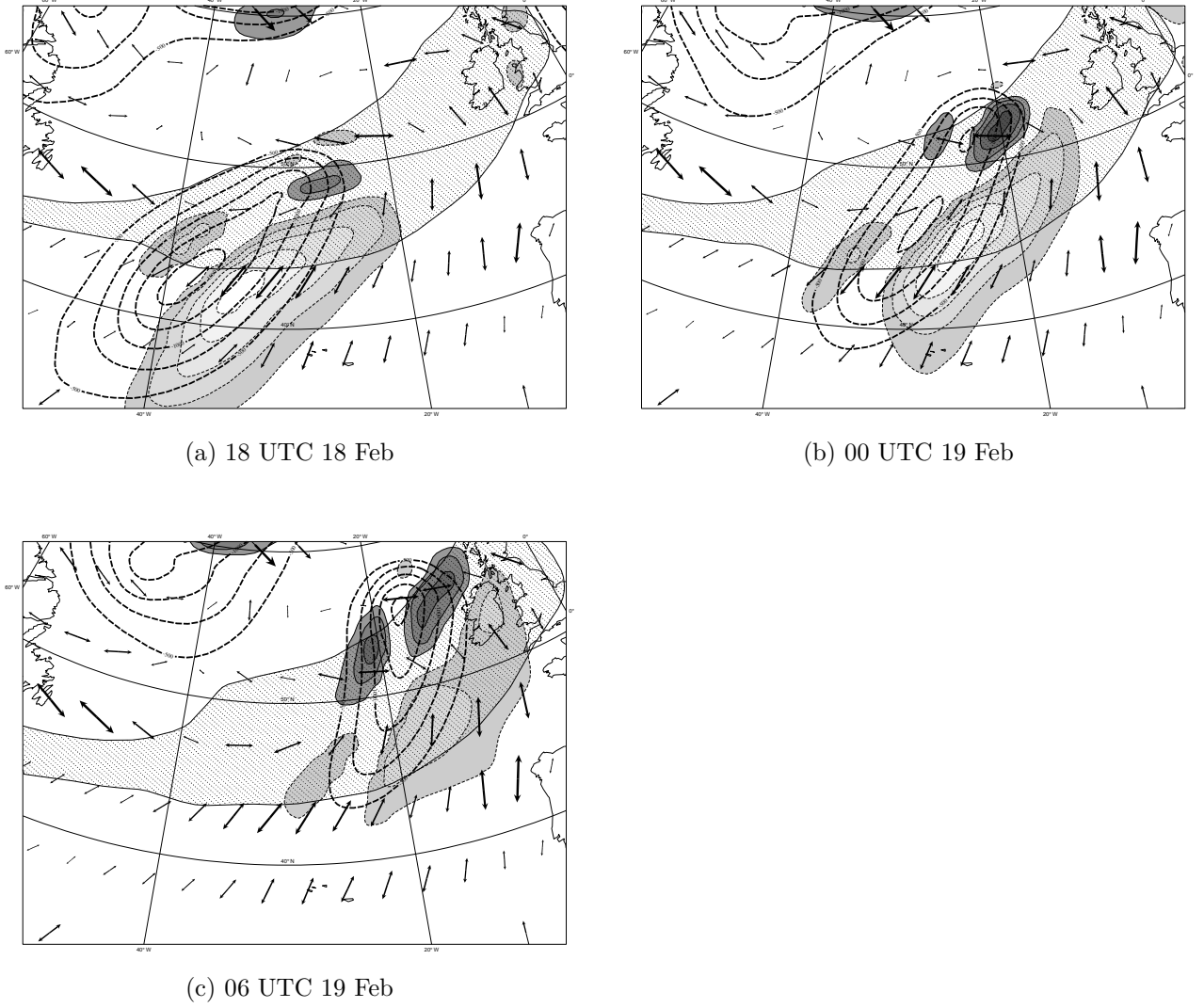
Figure 7: Barotropic generation rate $\mathbf{E}.\mathbf{D} - K'_e(\nabla_{\mathbf{p}}.\mathbf{u_m})$ at 900 hPa (contour interval is 1.5 $m^2.s^{-3}$, light shadings with dashed contours and dark shadings with solid contours indicate respectively negative values smaller than -1.5 $m^2.s^{-3}$ and positive values greater than 1.5 $m^2.s^{-3}$), low-frequency wind speed $|\mathbf{u_m}|$ at 900 hPa larger than 18 $m.s^{-1}$ (dotted shadings), high-frequency geopotential at 900 hPa smaller than -250 $m^2.s^{-2}$ (thick dashed contours, interval 250 $m^2.s^{-2}$) and dilatation axes at 900 hPa: (a) 18 UTC 18 Feb, (b) 00 UTC 19 Feb and (c) 06 UTC 19 Feb.
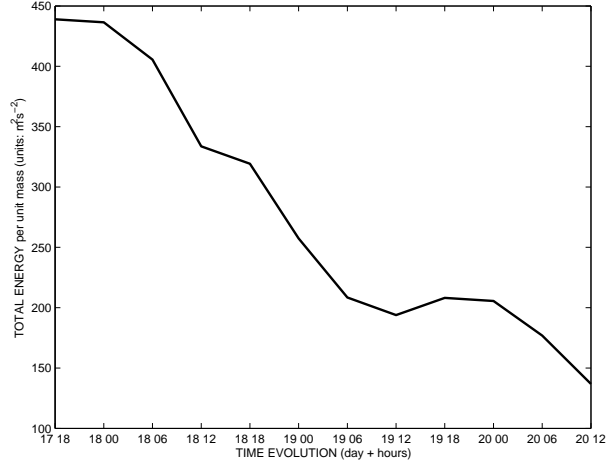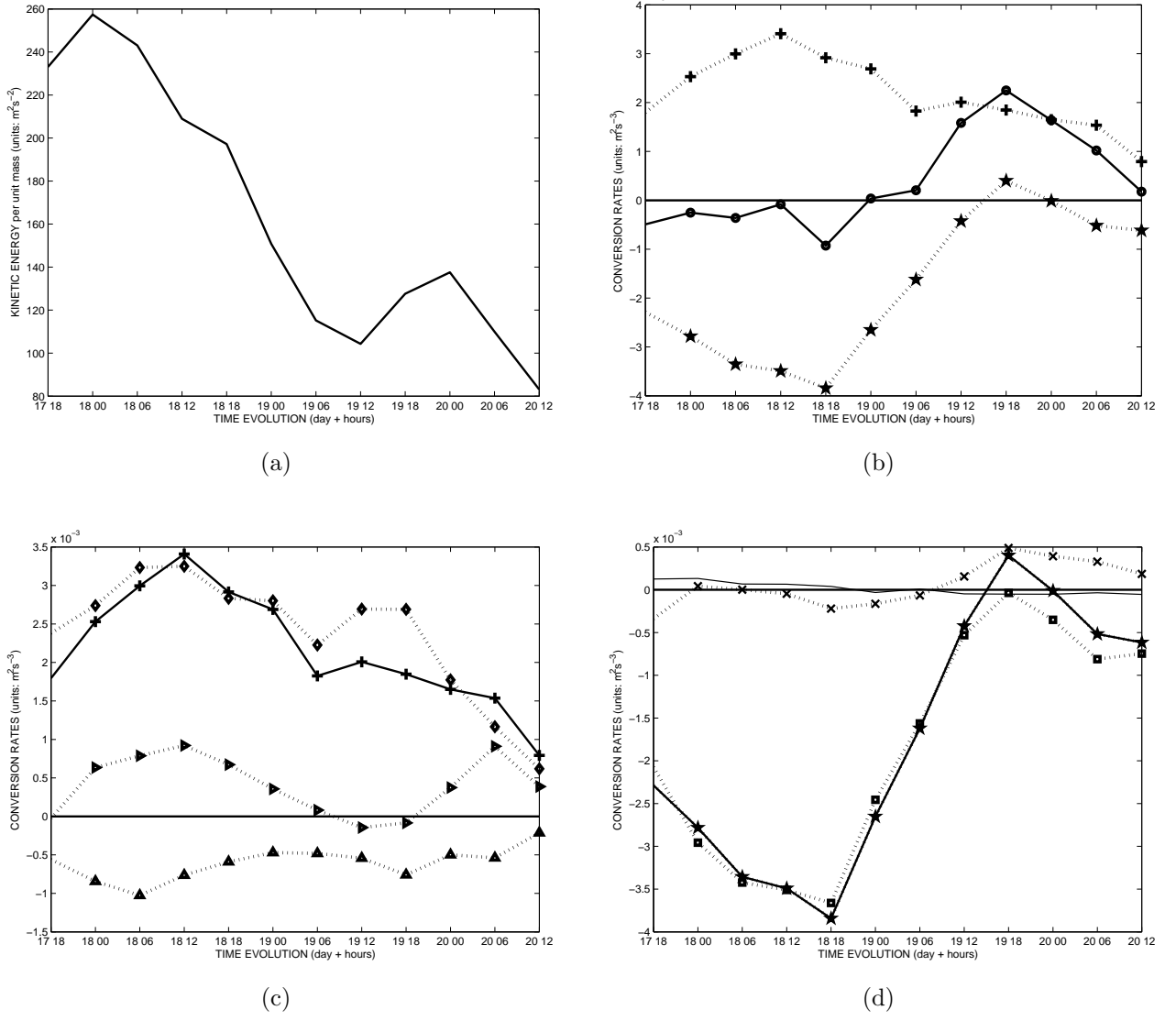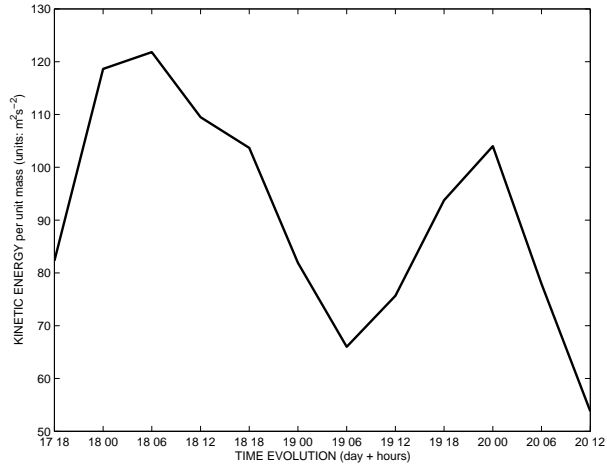
(a)
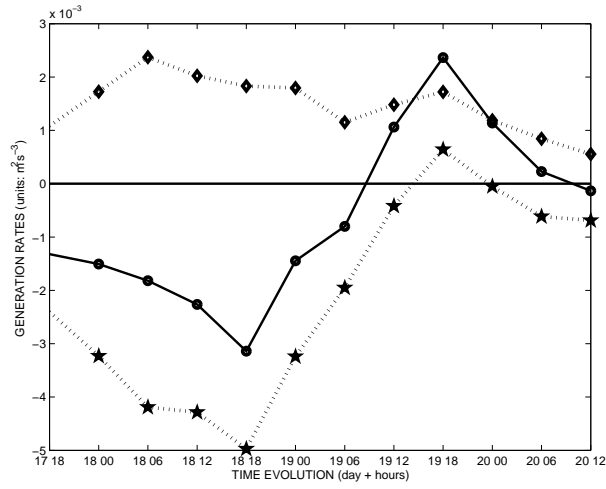
(b)

Figure 8: Time evolution of volume integrals over IOP17 between 200 and 900 hPa; (a) total energy T'_e per unit mass (solid line, units: $m^2.s^{-2}$), (b) baroclinic potential energy generation rate $\mathbf{F.B_c}$ (dotted line with diamonds) and Reynolds stress term $-\mathbf{u'}.(\mathbf{u'_3}.\nabla_\mathbf{3}\mathbf{u_m})$ (dotted line with stars) and sum of the two terms (solid line with circles)(units: $m^2.s^{-3}$). The volume is composed of a cylinder centred over the barycenter of T'_e computed around IOP17.

45

Figure 9: Time evolution of volume integrals over IOP17 between 200 and 900 hPa; (a) kinetic energy K'_e per unit mass (solid line, units: m^2.s^{-2}), (b) pressure work $-\mathbf{u}'.\nabla_{\mathbf{p}}.\Phi'$ (dotted line with + signs), Reynolds stress term $-\mathbf{u}'.(\mathbf{u}'_{\mathbf{3}}.\nabla_{\mathbf{3}}\mathbf{u}_{\mathbf{m}})$ (dotted line with stars) and the sum of the two terms (solid line with circles), (c) ageostrophic geopotential horizontal flux $-\nabla_{\mathbf{p}}.(\mathbf{u}'\Phi')$ (dotted line with ▶ signs), ageostrophic geopotential vertical flux $-\frac{\partial(\omega'\Phi')}{\partial p}$ (dotted line with ▲ signs), baroclinic conversion rate from potential to kinetic energy $-\mathcal{R}\theta'\omega'$ (dotted line with diamonds) and total pressure work $-\mathbf{u}'.\nabla_{\mathbf{p}}.\Phi'$ (solid line with + signs), (d) the barotropic generation rate $\mathbf{E}.\mathbf{D_m}$ (dotted line with squares), the divergence term $-K'_e(\nabla_{\mathbf{p}}.\mathbf{u_m})$ (thin solid line), vertical part of the Reynolds stress $\omega'(\mathbf{u}'.\frac{\partial \mathbf{u_m}}{\partial p})$ (dotted line with crosses) and the total Reynolds stress term $-\mathbf{u}'.(\mathbf{u}'_{\mathbf{3}}.\nabla_{\mathbf{3}}\mathbf{u_m})$ (solid line with stars) (growth rate units: m^2.s^{-3}). The volume is composed of a cylinder centred over the barycenter of K'_e computed around IOP17.
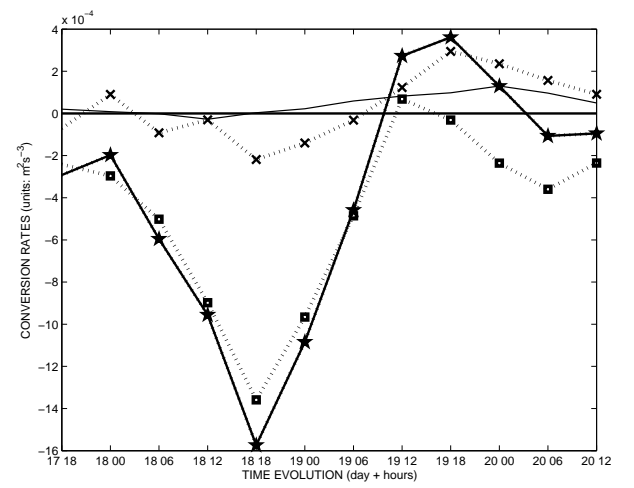
46

(a)
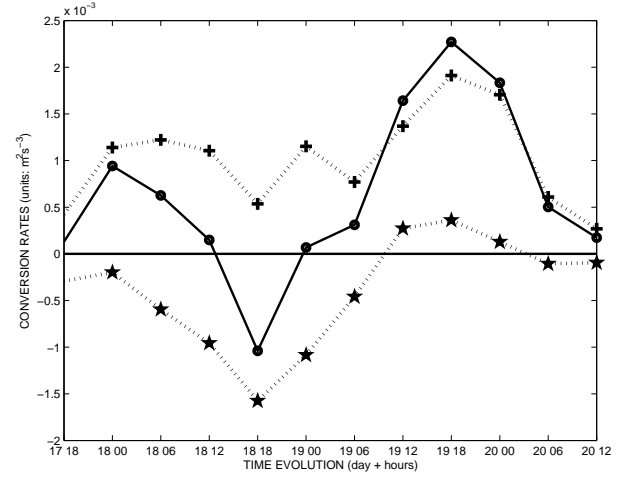
(b)
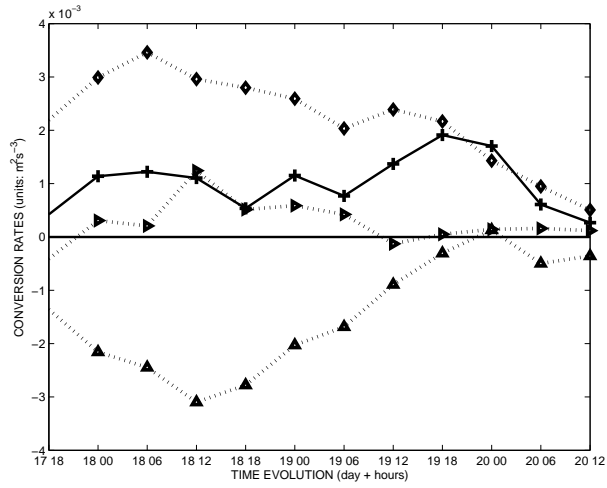
(c)

(d)

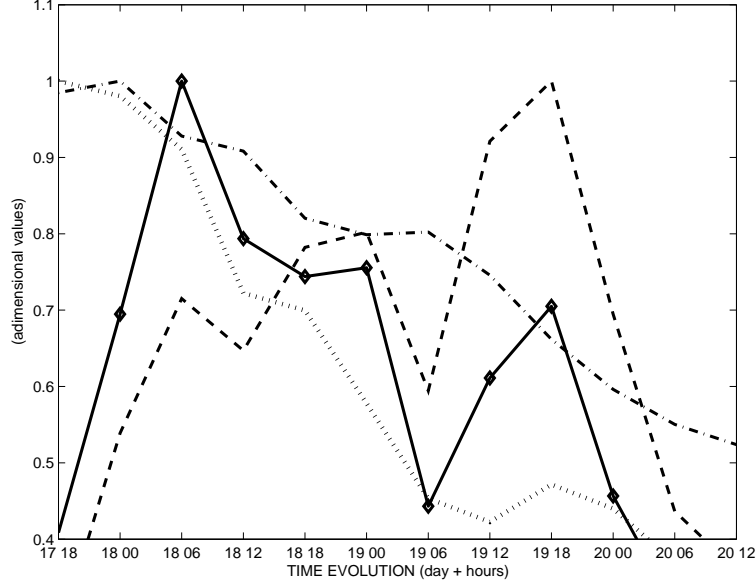Figure 10: Same as Fig.9, but for volume integrals over IOP17 between 600 and 900 hPa.

Figure 11: Time evolution of volume integrals over IOP17 between 200 and 900 hPa of the baroclinic generation rate $\mathbf{F}.\mathbf{B_c}$ (thick solid line with diamonds), the low-frequency baroclinicity $|\mathbf{B_c}|$ (dash-dotted line), the high-frequency total energy T'_e per unit mass (dotted line) and the configuration term $\mathbf{F}.\mathbf{B_c}/T'_e = |\mathbf{B_c}|.conf$ (dashed line). Each integrated variable is divided by its maximum during the period from 18 UTC 17 February to 12 UTC 20 February in order to compare its evolution to other variables. The volume is composed of a cylinder centred over the barycenter of $|\mathbf{F}.\mathbf{B_c}|$ computed around IOP17.
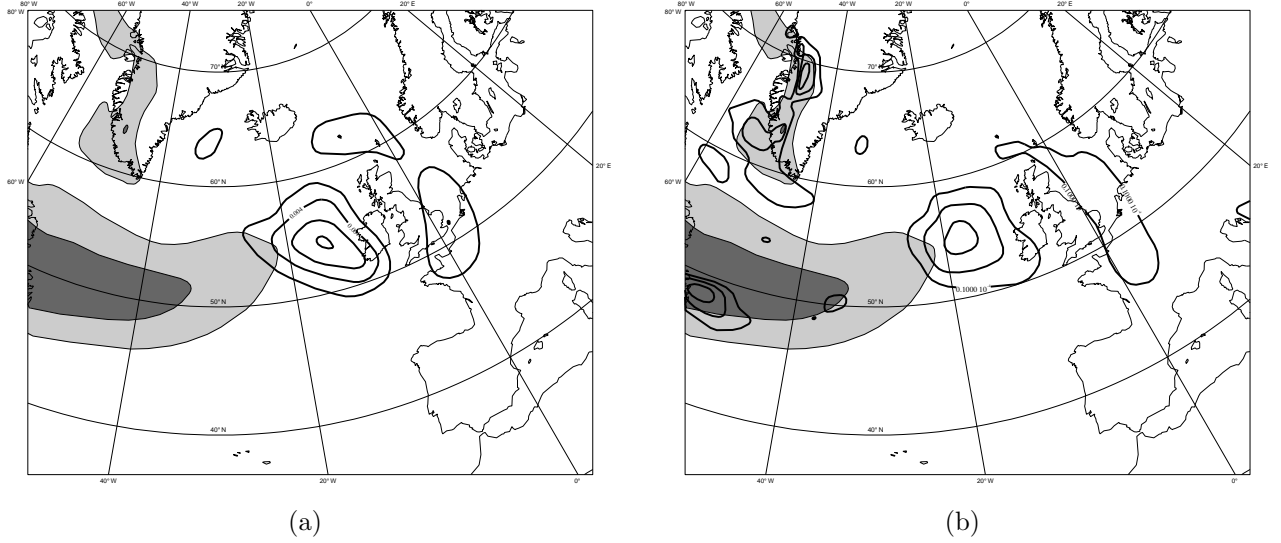
(a)

(b)

Figure 12: Vertically averaged (900-200hPa) low-frequency baroclinicity $|\mathbf{B_c}|$ larger than 3.10^{-5} s^{-1} (shaded contours, interval 10^{-5} s^{-1}) with (a) the vertically averaged (900-200hPa) baroclinic generation rate $\mathbf{F.B_c}$ larger than 2 m^2.s^{-3} (thick solid contours, interval 2 m^2.s^{-3}) and (b) the vertically averaged (900-200hPa) exponential baroclinic total energy generation rate $\mathbf{F.B_c}/T'_e$ larger than 10^{-5}s^{-1} (thick solid contours, contour interval 5.10^{-6}s^{-1}) at 18 UTC 19 February.